https://doi.org/10.5194/egusphere-2026-6104
Preprint. Discussion started: 5 November 2026
© Author(s) 2026. CC BY 4.0 License.

Mesospheric Gravity Waves in the OH Airglow Layer Generated by Winter Convection during an East Asian Winter Storm

Masaru Kogure[1], In-Sun Song[1], Hosik Kam[2]

[1]Department of Atmospheric Science, Yonsei University, Seoul, 03722, South Korea
[2]Center for Space Situational Awareness, Division of Space Information Research, Korea Astronomy and Space Science Institute, Daejeon 34055, Republic of Korea

Correspondence to: Masaru Kogure (masarukogure@yonsei.ac.kr)

Abstract. Gravity waves (GWs) are small-scale disturbances that play an important role in transporting momentum and energy from the lower to the upper atmosphere. Because mesospheric GWs can be observed far from their sources, event-resolved studies linking them to their tropospheric sources remain limited, particularly for midlatitude wintertime. Here, we investigate GWs associated with wintertime convection over East Asia during the winter storm of 24 January 2024. The Atmospheric Infrared Sounder (AIRS) and the Atmospheric Waves Experiment (AWE) observed semi-concentric GW patterns with horizontal wavelengths of several hundred kilometers in the stratosphere at ~05 UT and in the mesosphere at ~12 UT, respectively. A convection-permitting simulation using the Weather Research and Forecasting (WRF) model reproduced GW structures up to an altitude of ~47 km that were similar to those observed by AIRS. The simulation linked their generation to convection within a cold front north of Hokkaido (~144°E, ~47°N). Backward ray tracing suggested source regions north of Hokkaido ($136-149$°E, $44-53$°N) for the stratospheric and mesospheric GWs, consistent with regions of possible deep convection identified in the Himawari-9 observations. The agreement among the observations, WRF simulation, and ray-tracing results supports the interpretation that primary GWs generated by wintertime convection could propagate into the upper mesosphere. Additionally, those primary GWs were possibly saturated above ~68 km, raising the possibility of secondary GW generation. These results highlight the difficulty of distinguishing primary and secondary GWs based solely on concentric mesospheric wave patterns, including under wintertime.

1 Introduction

Gravity waves (GWs) are generated by meteorological disturbances, propagate upward with increasing amplitudes, and may reach the stratosphere, mesosphere, thermosphere, and ionosphere (Fritts and Alexander, 2003). When wave breaking occurs, the GWs deposit momentum and energy into the background flow, thereby driving atmospheric circulation

https://doi.org/10.5194/egusphere-2026-6104
Preprint. Discussion started: 5 November 2026
© Author(s) 2026. CC BY 4.0 License.

and affecting the temperature structure and distribution of chemical species (Lindzen, 1981; Matsuno, 1982; Holton, 1983; Butchart et al., 2011; Garcia et al., 2017).

One of the major sources of GWs is deep convection. Three mechanisms by which deep convection generates GWs have been proposed: pure thermal forcing, an obstacle effect, and a mechanical oscillator effect (Fritts and Alexander, 2003). While all three mechanisms can generate concentric or semi-concentric GWs, the obstacle and mechanical oscillator effects introduce directionality into GW spectra, depending on background wind shear at the altitude of deep convection. After GWs are emitted from deep convection, stratospheric and mesospheric winds can filter the GWs, induce wave breaking, and modify their spectra and spatial structures. In addition, GW breaking can induce a local body force that generates semi-concentric secondary GWs capable of propagating to higher altitudes (Vadas and Becker, 2019). Because these secondary GWs can exhibit spatial structures similar to those of primary GWs generated directly by convection, distinguishing the two types of GWs in the mesosphere is challenging (Vadas and Azeem, 2021; Kogure et al., 2026).

Despite this challenge, several observational studies have successfully linked mesospheric GWs with deep convection (Taylor and Hapgood, 1988; Sentman et al., 2003; Yue et al., 2009; Suzuki et al., 2007; Vadas et al., 2009; Nyassor et al., 2021; 2022; Li et al., 2025). For example, Nyassor et al. (2022) observed concentric GWs with a ground-based OH airglow imager and simultaneously identified a mesoscale convective system using observations from the Geostationary Operational Environmental Satellite (GOES). They applied a backward ray tracing method to the mesospheric GWs and suggested that the GWs originated from the mesoscale convective system. These event studies have focused primarily on the tropics or the summer midlatitudes, whereas event-resolved observational evidence linking mesospheric GWs to midlatitude wintertime convection remains limited.

Favorable atmospheric conditions for winter convection in extratropical regions are usually different from those for summer and tropical convection (Clark, T. L. 1986; Fovell et al., 1992; Piani et al., 2000; Clark M. R., 2009, 2013; Gatzen, 2011; Celiński-Mysław and Matuszko, 2014; Púčik et al., 2015; Mathias et al., 2019; Celiński-Mysław et al., 2020). In tropical regions and the summer extratropics, strong solar heating, together with abundant moisture, can destabilize the lower atmosphere and promote deep convection. The resulting potential for buoyant ascent is commonly quantified by convective available potential energy (CAPE), and high CAPE is often regarded as indicating an environment favorable for strong convective activity. Previous studies of convectively generated mesospheric GWs have primarily examined high-CAPE convective systems (Vadas et al., 2009, 2012; Nyassor et al., 2021, 2022). In contrast, in winter, convection often occurs within cold fronts under conditions of low-CAPE and high wind shear (Gatzen, 2011; Celiński-Mysław and Matuszko, 2014; Ludwig et al., 2015; Sherburn and Parker, 2014; Sherburn et al., 2016; King et al., 2017; De Orla-Barile et al., 2022). Synoptic-scale updrafts lift air parcels, causing water vapor to condense. The associated latent heating increases buoyancy and accelerates the parcels upward, while high wind shear can accelerate a rotation of the convective system. Thus, CAPE alone is insufficient for identifying the occurrence and intensity of wintertime convection. Outgoing longwave radiation (OLR) is also often used as a proxy for convection, particularly in studies of convectively generated GWs in the stratosphere

https://doi.org/10.5194/egusphere-2026-6104
Preprint. Discussion started: 5 November 2026
© Author(s) 2026. CC BY 4.0 License.

in tropical and subtropical regions. However, Cao and Liu (2022) noted that low OLR may not accurately represent convective activity at midlatitudes in winter.

Numerical simulation studies have shown that intense GWs in the stratosphere, mesosphere, and thermosphere often appear above cloud tops in storm-track regions ($30-50°$ N/S), where extratropical cyclone activity is high in the winter hemisphere (Choi and Chun, 2011, 2013; Kang et al., 2017; Song and Chun, 2005; Kogure et al., 2024). However, some of these studies used coarse-resolution general circulation models with convectively generated GW parameterizations. These models did not explicitly resolve convection, which may introduce uncertainty into the inferred GW sources. A few statistical observational studies have reported high GW activity over the storm-track regions and suggested that the high activity was attributable to convection within extratropical cyclones (Ern et al., 2011; Song et al., 2021; Kogure et al., 2025b). However, statistical analyses cannot fully separate the contribution of convection from the contributions of other GW sources, including spontaneous adjustment, orographic forcing, and secondary GW generation. Moreover, GW activity is modulated by propagation conditions and wind filtering between the source and the observation altitude. Thus, although modeling and statistical studies suggest that winter storm tracks are important source regions of convectively generated GWs, event-resolved observational evidence linking individual wintertime convective systems to GWs remains limited, especially GWs in the mesosphere and thermosphere.

This study investigates whether mesospheric GWs observed during a midlatitude winter storm can be linked to a tropospheric convective source. We analyze semi-concentric GWs observed in the stratosphere and the OH airglow layer during the East Asian winter storm of 24 January 2024 by combining spaceborne observations, a convection-permitting meteorological simulation, and ray tracing. Section 2 describes the observational data, numerical simulation, and analysis methods. Section 3 presents the meteorological conditions, the stratospheric and mesospheric GW observations, the simulated GW fields, and the ray tracing results linking the observed GWs to deep convection during the winter storm. Section 4 discusses possible alternative sources and evaluates the robustness and limitations of the inferred source connection. Section 5 summarizes the principal findings and conclusions.

2 Data and methodology

2.1 Observations and analysis

2.1.1 Himawari-9 and deep convection analysis

We used the Japan-area observation dataset from Himawari-9, a Japanese geostationary meteorological satellite (Bessho et al., 2016), to examine the meteorological conditions during the winter storm. Himawari-9 has 16 observation bands ranging from 0.47 to 13.3 μm. We analyzed brightness temperatures from Bands 8 ($T_{6.2}$) and 13 ($T_{10.4}$), corresponding to wavelengths of 6.2 and 10.4 μm, respectively, to identify convective activity. The Japan-area data have a spatial resolution of 2 km and a temporal resolution of 2.5 min. The data were obtained from the Data Integration and Analysis System Program (DIAS), operated by the Japan Agency for Marine-Earth Science and Technology (JAMSTEC).

https://doi.org/10.5194/egusphere-2026-6104
Preprint. Discussion started: 5 November 2026
© Author(s) 2026. CC BY 4.0 License.

In accordance with the Users' Guide provided by JMA (JMA, 2015), brightness temperatures from these two bands are used to identify deep convective areas based on the following criterion: a positive brightness-temperature difference between $\boldsymbol{T_{6.2}}$ and $\boldsymbol{T_{10.4}}$ indicates that cloud tops may overshoot into the stratosphere. We used the difference between $\boldsymbol{T_{6.2}}$ and $\boldsymbol{T_{10.4}}$ ($\boldsymbol{T_{6.2} - T_{10.4}}$) as an indicator of deep convective activity.

2.1.2 Atmospheric Infrared Sounder (AIRS)

AIRS is an instrument aboard NASA's Aqua satellite that measures infrared radiance spectra in three spectral bands between 3.7 and 15.5 μm (Aumann et al., 2003; Chahine et al., 2006). Aqua is in a sun-synchronous orbit at an altitude of ~705 km, completes one orbit every 99 min, and crosses nearly the same geographical location twice daily at ~01:30 LT and ~13:30 LT. These local times over South Korea and Japan correspond to ~17 and ~05 UT, respectively. AIRS scans Earth's atmosphere, with each scan consisting of 90 footprints that cover 1,780 km in the cross-track direction and 18 km in the along-track direction. The footprint size ranges from 14×14 km^2 at nadir to 21×42 km^2 at the scan edges, yielding a Nyquist horizontal wavelength of 30–80 km. We analyzed dedicated AIRS 4 μm brightness-temperature datasets as well as 3-D stratospheric temperature retrievals. Both datasets were provided by the Jülich Supercomputing Center, Germany (Hoffmann, 2021). These datasets were used to examine temperature perturbations associated with stratospheric GWs.

2.1.3 GW analysis of AIRS

To extract GW perturbations from AIRS data, background temperatures were estimated using a fourth-order polynomial fit and then subtracted from the brightness temperatures in each across-track scan. The residuals were defined as temperature perturbations primarily associated with GWs with horizontal wavelengths greater than ~80 km and up to several hundred kilometers. For the 4 μm brightness-temperature perturbations, measurement noise was reduced by vertically averaging radiances from multiple AIRS channels. The vertical kernel peaks at an altitude of ~35 km and has a full width at half maximum of ~20 km. Because of the vertical sensitivity of the kernel, 4 μm brightness temperature perturbations primarily represent GWs with vertical wavelengths longer than ~20 km and can substantially underestimate their temperature amplitudes. We applied 2-D Lomb-Scargle spectral analysis to 4 μm brightness temperature perturbations to obtain the GW horizontal wavelength spectra in the stratosphere. We determined the full width at half maximum (FWHM) of each spectral power peak in the two-dimensional horizontal-wavenumber spectrum and obtained the corresponding ranges of horizontal wavelength and azimuth angle. For the 3-D retrieved stratospheric temperature, we analyzed the 3-D perturbations along each latitude to investigate their vertical wavelengths. To suppress noise and clarify the westward-propagating GWs with long horizontal wavelengths, we applied a low-pass filter with a longitudinal cutoff wavelength of 3° (~230 km at 47°N).

https://doi.org/10.5194/egusphere-2026-6104
Preprint. Discussion started: 5 November 2026
© Author(s) 2026. CC BY 4.0 License.

Details of the AIRS observations and retrieval methodology for 3-D retrieved stratospheric temperature fields and 2-D GW perturbations are described in Hoffmann and Alexander (2009) and Hoffmann et al. (2013, 2014, 2016, 2017).

2.1.4 Atmospheric Waves Experiment (AWE)

AWE operates an Advanced Mesospheric Temperature Mapper (AMTM), a nadir-viewing instrument mounted at the ELC1 site on the International Space Station (ISS). The AMTM combines infrared detector technology with high-throughput optical systems to provide high-quality temperature maps (Pautet et al., 2014). It is composed of a four-channel infrared imager that measures spectral emissions of the hydroxyl (OH) nightglow. Each of the instrument's four identical telescopes has a unique spectral filter to detect three OH emission lines, $P_1(2)$, $P_1(4)$, and $Q_1(1)$ of the OH (3, 1) band, and background brightness. OH nightglow emissions typically originate from a layer near 87 km, with a FWHM of ~10 km (Baker and Stair, 1988). Therefore, the AWE AMTM is sensitive mainly to waves with vertical wavelengths longer than the OH layer thickness (~10 km). Temperatures at ~87 km are derived from the four brightness signals. Images are collected continuously at approximately one image per second with a horizontal resolution of 2 km (Lamborn et al., 2024). The ISS completes ~15.5 orbits per day, with successive orbits separated by ~1.5 h. The orbit shifts by ~6° in longitude per day and by ~23 min in local time.

This study uses orbital keograms of $Q_1(1)$ radiance and temperature. The $Q_1(1)$ emission line is less sensitive to cloud-reflected emissions because of strong water vapor absorption at the same wavelength, although some contamination from high-altitude clouds associated with deep convection may still be present in the images. For each orbit, the swath data are ~600 km wide and ~15,000 km long, with horizontal resolutions of 2 km for the $Q_1(1)$ emissions and 10 km for the mesospheric temperatures. The AWE datasets are provided by Utah State University.

2.1.5 GW analysis of AWE

To derive GW perturbations from AWE, we first applied a Gaussian smoothing filter, with a FWHM of 600 km and a 2400 km window size, along each orbit and subtracted the smoothed values from the original values. A second-order bilinear fit was applied to the residuals in a target area, and the fitted values were subtracted from the residuals. We defined the final residuals as GW perturbations. To obtain the GW spectra in the upper mesosphere, we applied 2-D Lomb-Scargle spectral analysis to the final residuals. We obtained the corresponding ranges of horizontal wavelength and azimuth angle using the same procedure as for AIRS. We identified robust peaks by examining their consistency between the $Q_1(1)$ radiance and temperature spectra.

2.2 Advanced Research Weather Research and Forecasting Model (WRF-ARW)

We conducted a weather simulation using version 4.7.1 of the WRF-ARW model (Skamarock et al., 2019) to investigate stratospheric GWs and the associated tropospheric weather conditions. The simulation was performed from 00 UT on January 23 to 00 UT on January 25, 2024, covering the Korean Peninsula and Japan's main and northern islands. Initial and lateral boundary conditions were obtained from the European Centre for Medium-Range Weather Forecasts

https://doi.org/10.5194/egusphere-2026-6104
Preprint. Discussion started: 5 November 2026
© Author(s) 2026. CC BY 4.0 License.

Reanalysis v5 (ERA5; Hersbach et al., 2020) on pressure coordinates. Our simulation used 90 eta levels extending from the surface to the model top at 1 hPa, corresponding to an altitude of ~47 km. The uppermost 5 km of the model domain was configured as a damping layer with a damping coefficient of 0.3. The vertical resolution ranges from ~100 to ~660 m, depending on altitude. We used a two-way nested domain configuration. Domains 1 and 2 consisted of 800×600 and 802×601 grid points, respectively, with horizontal resolutions of 9 and 3 km, respectively (see Figure A1 in the Appendix). The time steps were 30 s for Domain 1 and 10 s for Domain 2. Cumulus convection parameterization (the Grell-Freitas scheme) and grid nudging toward ERA5 were enabled in Domain 1. The nudging followed WRF's default configuration, with a nudging coefficient of 3.3×10^{-4} s^{-1} for horizontal winds, temperature, and moisture within Domain 1. The ERA5 fields used for nudging were updated every hour. In contrast, cumulus parameterization and nudging were both turned off in Domain 2 because its 3 km resolution is within the convection-permitting range commonly used to explicitly resolve convective systems, although some convective processes remain under-resolved (Weisman et al., 1997; Bryan et al., 2003; Prein et al., 2015; Wang et al., 2021). The other parameters were set up following the WRF user guide; that is, the Thompson microphysics, RRTMG longwave and shortwave radiation, MYJ planetary boundary layer, and Noah land-surface schemes were employed. For this study, we analyzed Domain 2 output at 5-min intervals on 24 January 2024.

2.2.1 GW analysis of WRF

To derive GW perturbations, we first subtracted the horizontal mean over Domain 2 from the raw field at each vertical level and then applied a first-order bilinear fit to the residuals. The fitted values were subtracted from the residuals. Finally, a Butterworth band-pass filter with lower and upper cut-off horizontal wavelengths of 80 and 750 km, respectively, was applied to the residuals. The resulting band-pass-filtered fields were defined as GW perturbations. We applied the AIRS vertical kernel to the simulated GW perturbations to facilitate comparison between the 4 μm brightness-temperature perturbations and WRF simulations. The kernel weights were set to zero above the WRF model top (~47 km) and overlapped the uppermost 5 km damping layer. Consequently, the effective vertical response differs from that of AIRS and could be sensitive to GWs with short vertical wavelengths, which limits quantitative comparison of the perturbation amplitudes. We mainly focus on both morphologies rather than the magnitude of amplitudes.

2.2.2 Analysis of Meteorological Conditions in WRF

We also briefly investigated the meteorological conditions during this winter storm. In addition to the fundamental meteorological output (temperature and water vapor), we calculated CAPE and storm relative helicity, which are widely used to assess convection, storms, and supercells with WRF-Python (Visualization and Analysis, 2017). The two parameters were calculated with the default settings. In the default settings, CAPE is accumulated from the maximum equivalent potential temperature height in the lowest 3 km to the level of free convection, while Storm relative helicity is calculated for the lowest 3 km layers above ground level.

https://doi.org/10.5194/egusphere-2026-6104
Preprint. Discussion started: 5 November 2026
© Author(s) 2026. CC BY 4.0 License.

2.3 GW ray-tracing method

To assess the propagation paths of the observed GWs from their sources to the stratosphere and mesosphere, we applied a ray-tracing method. Our ray tracing method follows the mathematical framework described by Marks and Eckermann (1995). To estimate the lowest height of potential wave saturation, our forward model calculates the growth of wave energy and wave action with height under nondissipative conditions using the inertial GW polarization relation (Geller and Gong, 2010). Details of our ray-tracing method are described in Kogure et al. (2018, 2020, 2023). The background atmospheric conditions were obtained from a reanalysis, JAWARA (Koshin et al., 2025), because JAWARA data are assimilated with observations up to an altitude of ~110 km. The parameters in JAWARA were trilinearly interpolated in longitude, latitude, and time, and then the trilinearly interpolated values were vertically interpolated. The initial parameters of stratospheric GWs were derived from AIRS observations. Because vertical averaging by the vertical kernel function can cancel GW amplitudes, we estimated the underlying temperature amplitudes by dividing the measured brightness-temperature amplitudes by a climatological response factor in winter midlatitudes. The response factor was obtained from Hoffmann (2021). These estimated amplitudes were input for the forward ray tracing. For the mesospheric GWs, the initial parameters were determined from the AWE $Q_1(1)$ relative radiance perturbations rather than the temperature perturbations because the former are less susceptible to cloud contamination. A backward ray may terminate at a critical level, a turning level, or the surface; its termination point does not necessarily identify the GW generation region.

3. Results

3.1 Meteorological conditions over Japan during the winter storm on 24 January 2024

Figure 1 shows the brightness-temperature difference between Himawari-9 Bands 8 and 13 at 02 and 05 UT. The differences were near 0 or positive in three regions: northeast of Hokkaido (~144 – 151°E, ~43 – 48°N), northern Tohoku (~138 – 142°E, ~40 – 42°N), and the Pacific Ocean near Tohoku (~144 – 147°E, ~35 – 40°N).

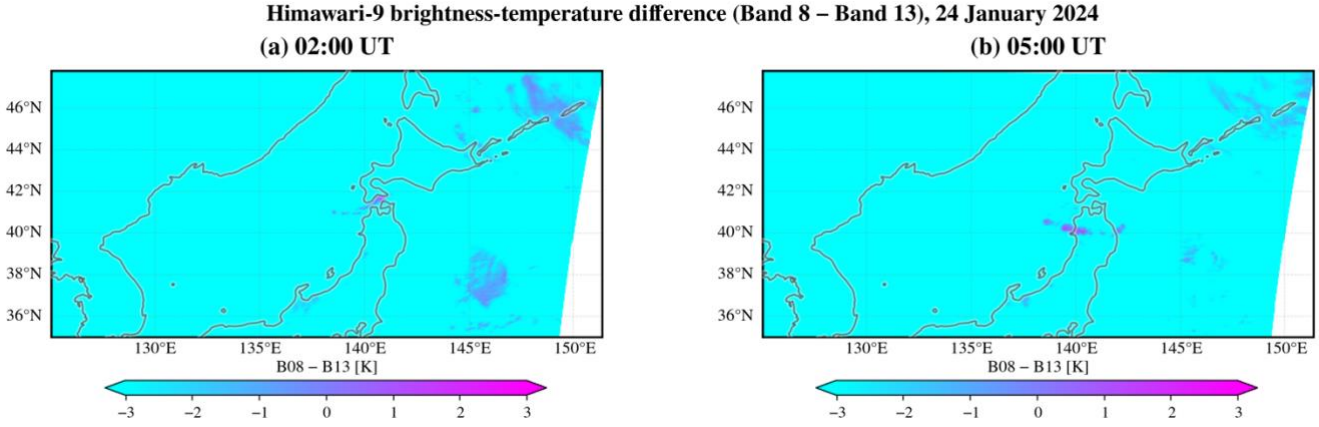


Figure 1. Brightness-temperature difference between Himawari-9 Bands 8 and 13 at 02 (a) and 05 (b) UT on 24 January 2024.

https://doi.org/10.5194/egusphere-2026-6104
Preprint. Discussion started: 5 November 2026
© Author(s) 2026. CC BY 4.0 License.

Figure 2 shows meteorological parameters related to deep convection at 02 UT in the WRF simulation. In Figure 2a, a cold air mass covered Primorsky Krai in Russia, northeastern China, Tohoku, and eastern Hokkaido in Japan (~35–48°N, ~130–145°E), and extended toward the Pacific Ocean near Tohoku (~35–40°N, ~140–150°E). In contrast, a warm air mass extended into eastern Hokkaido from the Pacific Ocean, accompanied by a cyclonic wind pattern. This pattern was associated with a temperature boundary, namely a cold front, extending from Hokkaido to the Pacific Ocean. Column water vapor in Figure 2b exhibited a curved distribution broadly following the cyclonic circulation in Figure 2a, with enhanced moisture extending from the Pacific Ocean toward northern Japan. The distributions of relatively warm and moist air and the strong temperature gradient broadly corresponded to the three regions of possible deep convection identified from Himawari-9, shown in Figures 1a and 1b.

https://doi.org/10.5194/egusphere-2026-6104
Preprint. Discussion started: 5 November 2026
© Author(s) 2026. CC BY 4.0 License.

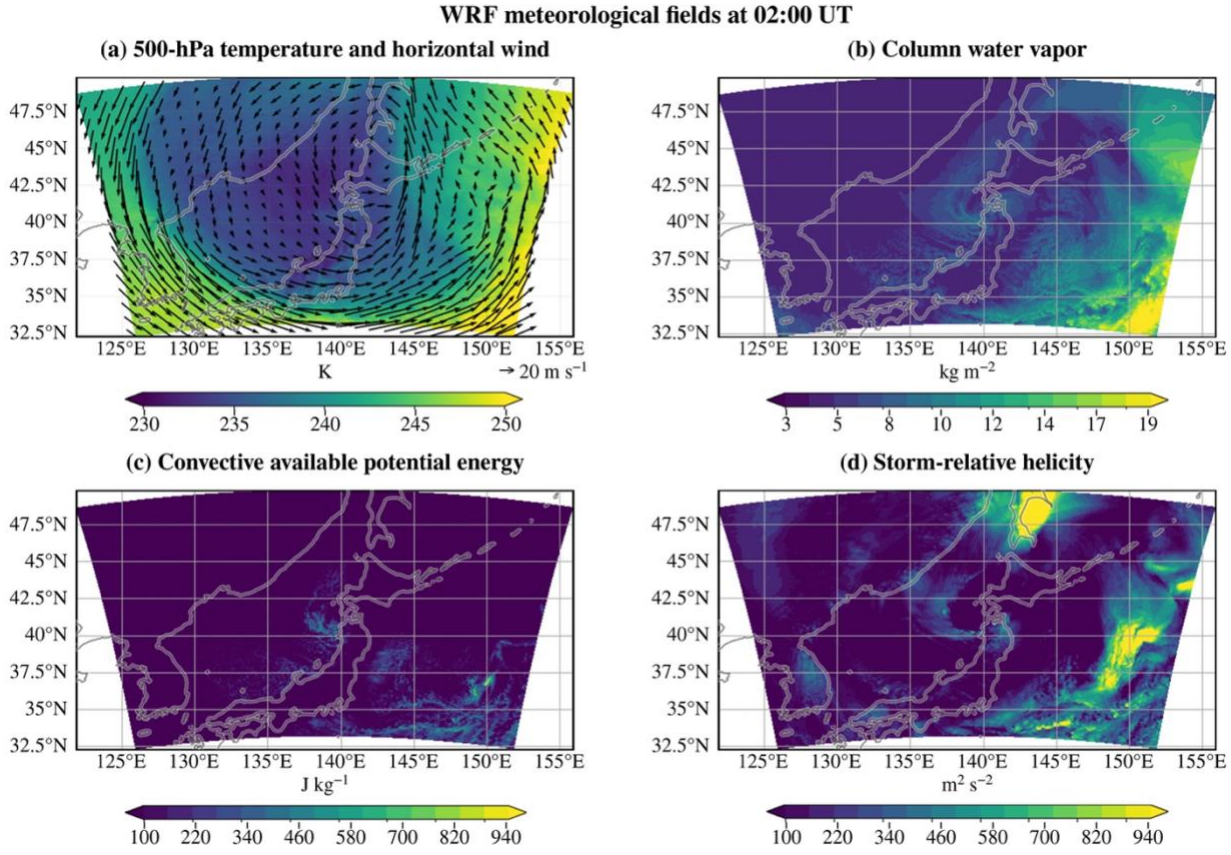


Figure 2. Temperature (color map) and wind (arrows) at 500 hPa (a), column water vapor (b), convective available potential energy (CAPE) (c), and storm relative helicity (d) in the WRF simulation at 02 UT on 24 January, 2024.

South of ~41°N, regions of relatively high CAPE in Figure 2c broadly coincided with enhanced column water vapor in Figure 2b and with the possible convective regions over northern Tohoku and the Pacific Ocean near Tohoku in Figure 1. However, CAPE remained below 1000 J kg^{-1} throughout almost all of WRF domain 2 and was particularly small around Hokkaido, where values north of 42°N were generally below 100 J kg^{-1} despite the presence of possible deep convection in the Himawari-9 observations. In contrast, storm-relative helicity in Figure 2d was enhanced, exceeding 500 m^2 s^{-2}, in northern Tohoku, (~40°N, ~141°E), north of Hokkaido (~46 − 49°N, ~140 − 145°E), and the Pacific Ocean (~35 − 43°N, ~147 − 152°E). These enhanced storm-relative helicity regions were located near the three regions of possible deep convection identified from Himawari-9, although their locations did not coincide exactly.

Taken together, the Himawari-9 observations and WRF simulation indicate that the three regions of possible deep convection were associated with the wintertime frontal system over and around Hokkaido, Tohoku, and the Pacific Ocean. These possible convective regions were characterized by relatively low CAPE and high storm-relative helicity, consistent with the low-CAPE, high-shear environments reported for cold-season convection in previous meteorological studies (Burke and

https://doi.org/10.5194/egusphere-2026-6104
Preprint. Discussion started: 5 November 2026
© Author(s) 2026. CC BY 4.0 License.

Schultz, 2004; Celiński-Mysław and Matuszko, 2014; Celiński-Mysław et al., 2020; Sherburn and Parker, 2014; Sherburn et al., 2016). These meteorological characteristics persisted throughout 24 January 2024.

3.2 Stratospheric and mesospheric GWs over the Korean Peninsula, northeast China, Khabarovsk Krai in Russia, and Japan during the winter storm

This section presents GWs observed by AIRS and AWE and describes their spatial structures.

3.2.1 Stratospheric GWs observed by AIRS

Figure 3 shows 4-μm brightness-temperature perturbations at ~35 km at 04:34–04:42 UT (Figure 3a) and 18:07–18:15 UT (Figure 3b). Semi-concentric GWs appeared over the Korean Peninsula, northeast China, Khabarovsk Krai, and Japan at 04:34–04:42 UT (Figure 3a). These semi-concentric structures are consistent with the characteristics of convectively generated GWs observed during the warm season (Yue et al., 2009; Vadas et al., 2012; Nyassor et al., 2022). Their apparent epicenter was located near (~47°N, ~148°E), close to the region of possible deep convection northeast of Hokkaido identified by Himawari-9 (Figure 1). Semi-concentric GWs also appeared at 18:07–18:15 UT, with an apparent epicenter located at (~43°N, ~145°E) (Figure 3b). The similarity of the structures observed at ~05 and ~18 UT suggests repeated GW activity associated with deep convection over the region north of Hokkaido ($\sim 43 - 48$°N, $\sim 144 - 151$°E). Figure 4 shows 2-D Lomb-Scargle spectra of the brightness-temperature perturbations. Both spectra show dominant peaks with horizontal wavelengths of ~400–650 km and azimuth angles of ~250–270°. It should be noted that, although the 2-D spectral analysis has a 180° ambiguity, we infer westward propagation from the wave morphology, particularly the dominance of the western portion of the semi-concentric wave pattern. Table 1 summarizes the first and second peaks.

https://doi.org/10.5194/egusphere-2026-6104
Preprint. Discussion started: 5 November 2026
© Author(s) 2026. CC BY 4.0 License.

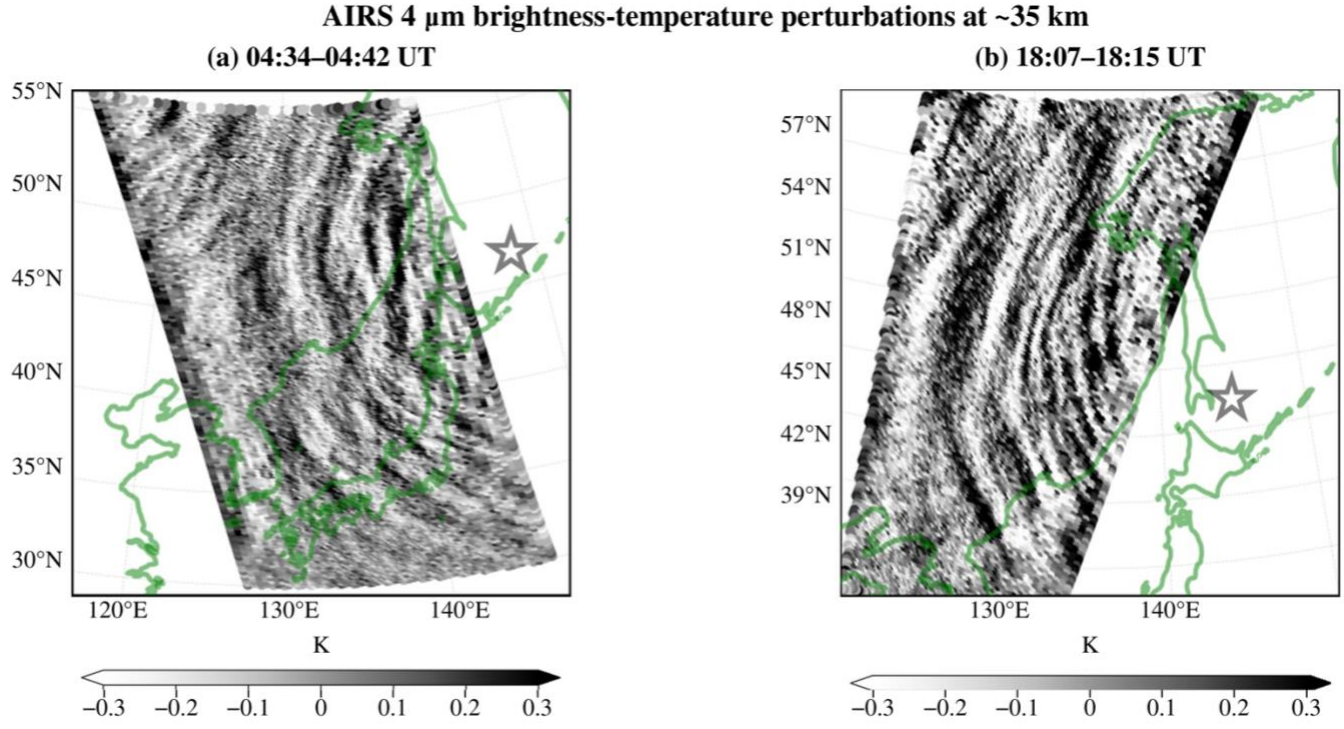


Figure 3. 4-μm brightness-temperature perturbations at ~35 km at 04:34–04:42 UT (a) and at 18:07–18:15 UT (b).

https://doi.org/10.5194/egusphere-2026-6104
Preprint. Discussion started: 5 November 2026
© Author(s) 2026. CC BY 4.0 License.

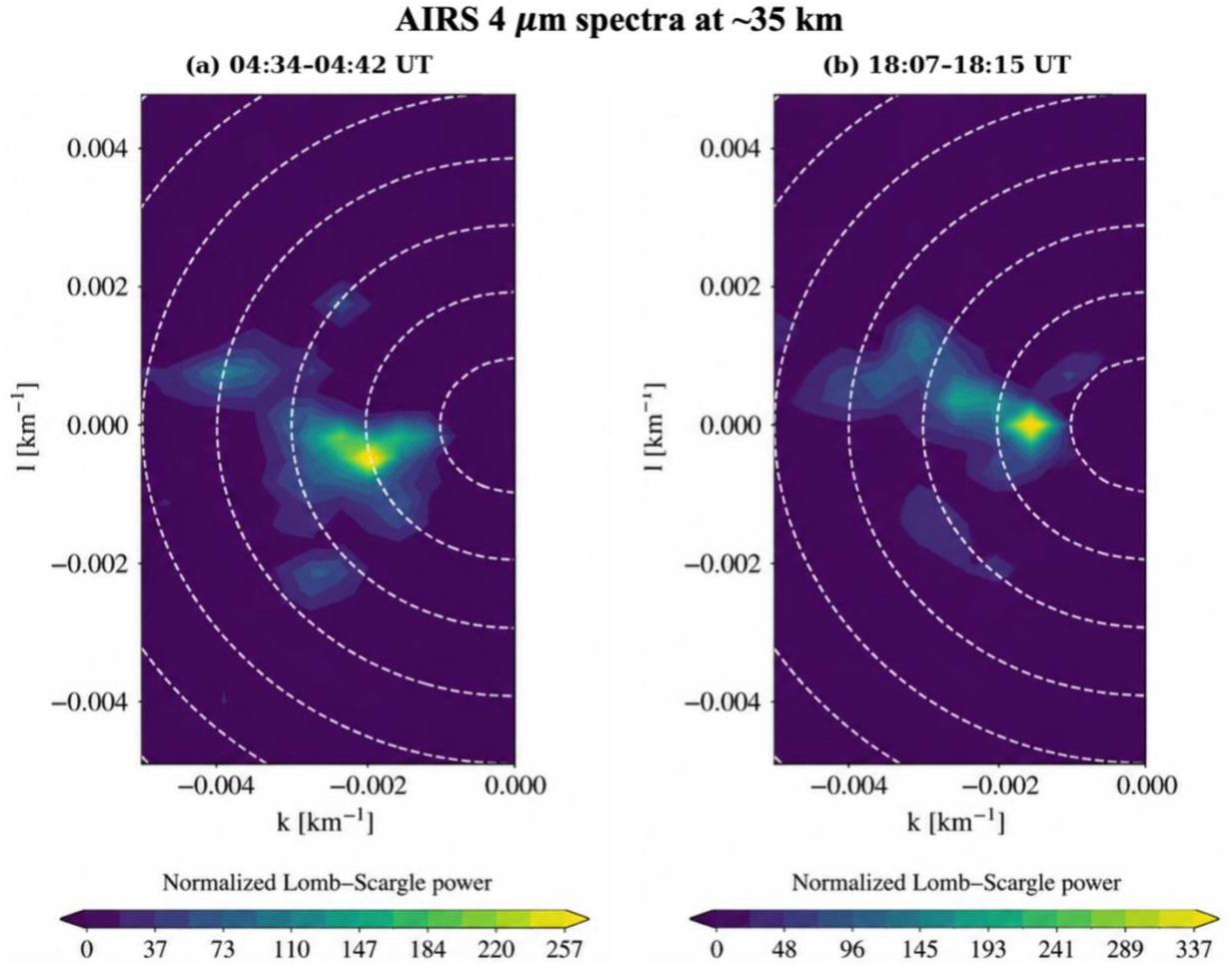


Figure 4. 2-D Lomb-Scargle spectra of the 4-μm brightness-temperature perturbations at ~35 km at 04:34–04:42 UT (a) and at 18:07–18:15 UT (b). White dashed lines denote 0.001 [km^{-1}] intervals.

https://doi.org/10.5194/egusphere-2026-6104
Preprint. Discussion started: 5 November 2026
© Author(s) 2026. CC BY 4.0 License.

Time	04:34–04:42		18:07–18:15	
	1st peak	2nd peak	1st peak	2nd peak
Azimuth angle [°]	256 (248–264)	266 (260–272)	270 (261–279)	262 (255–270)
Horizontal wavelength [km]	498 (394–680)	426 (358–488)	648 (510–851)	385 (330–451)

Table 1. 1st and 2nd peaks of the Lomb-Scargle spectra in AIRS. Values in parentheses indicate the parameter ranges corresponding to the full width at half maximum of each spectral peak. Azimuth angles are measured clockwise from north.

At ~05 UT, the WRF simulation reproduced prominent GW structures propagating westward from the region north of Hokkaido (~140–150°E, 43–48°N), broadly consistent with the spatial scales and propagation direction observed by AIRS (Figure 3a and 5a, b). The simulated GWs propagated westward from the region north of Hokkaido between 00 and 19 UT (Movie 1 and Movie 2 in the supplement). By ~18 UT, however, the simulated amplitudes had substantially decreased, and the wave structures became less distinct, unlike the pronounced GWs observed by AIRS at ~18 UT.

https://doi.org/10.5194/egusphere-2026-6104
Preprint. Discussion started: 5 November 2026
© Author(s) 2026. CC BY 4.0 License.

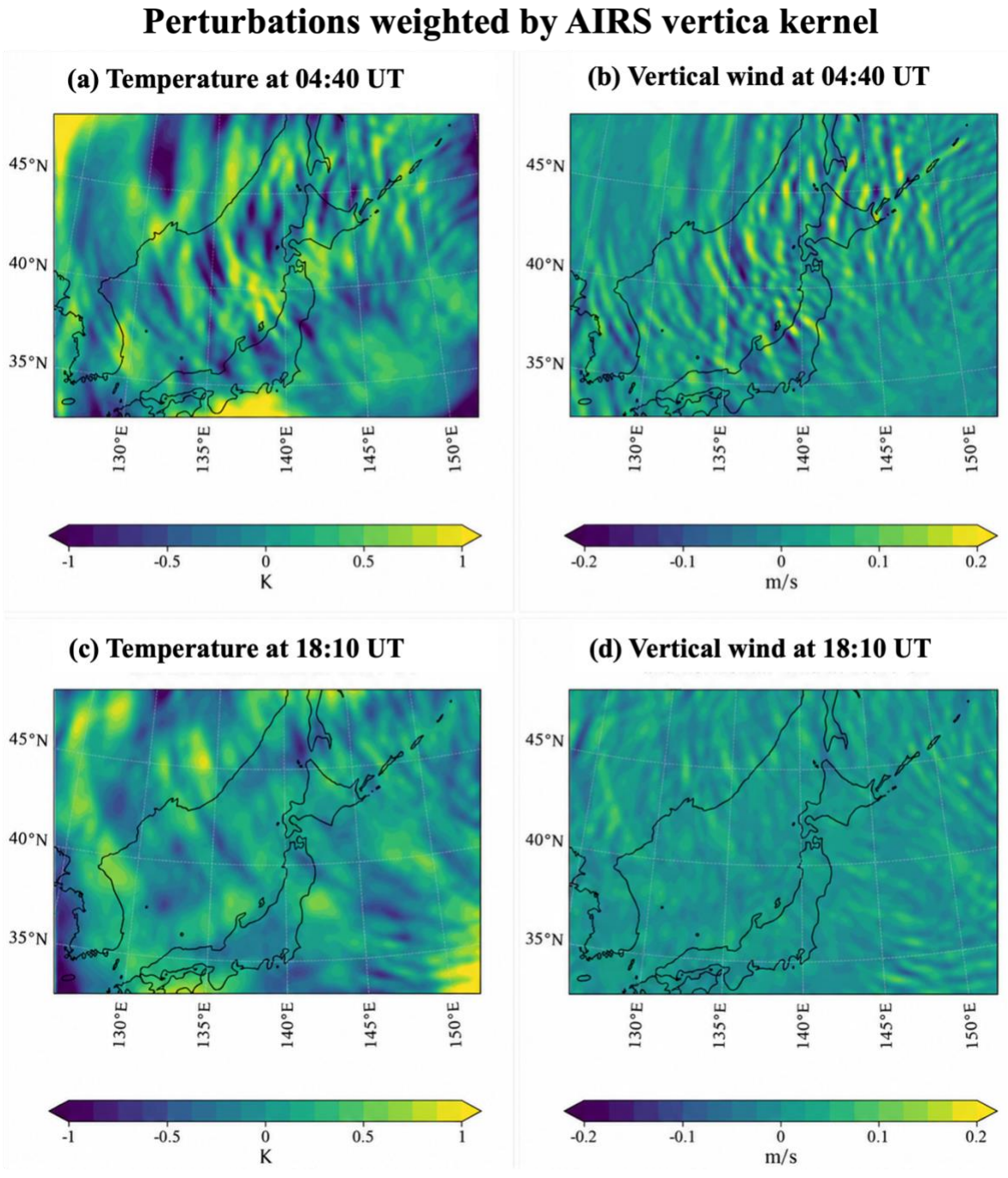


Figure 5. Temperature and vertical wind perturbations of GWs with horizontal wavelengths of 80–750 km. These values were vertically averaged with the AIRS 4 μm kernel function. Note that the kernel weights were set to zero above the model top (~47 km).

https://doi.org/10.5194/egusphere-2026-6104
Preprint. Discussion started: 5 November 2026
© Author(s) 2026. CC BY 4.0 License.

Figure 6 shows longitude-vertical cross-sections of AIRS 3-D retrieved temperature perturbations. The retrieved temperature perturbations exhibit clear phase tilts with altitude. The phase tilts are consistent with upward energy propagation for the inferred westward propagation direction. The GWs had zonal wavelengths of ~3–8° (~230–600 km) and vertical wavelengths of ~25–30 km at both times.

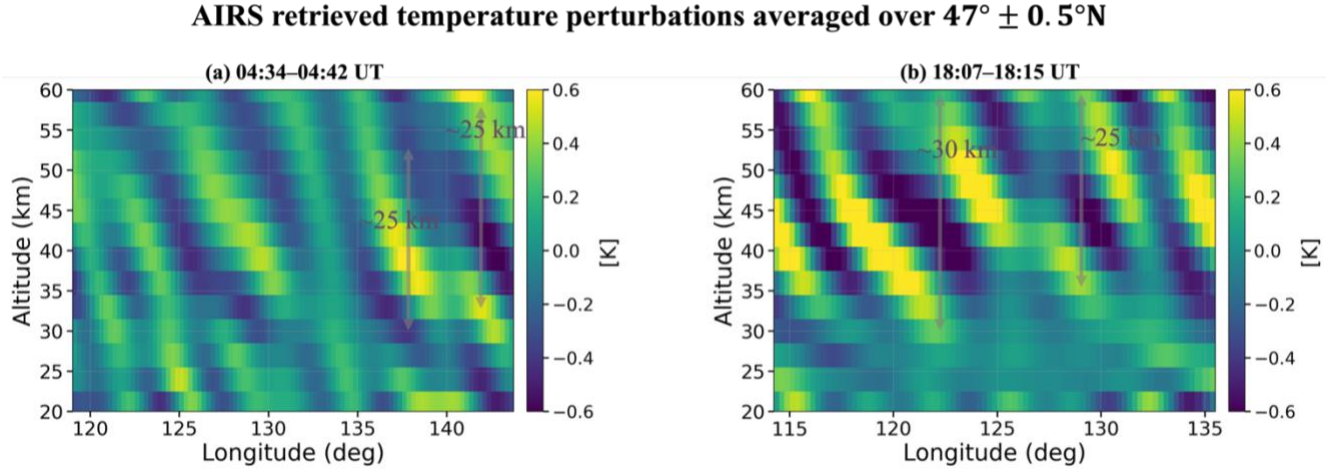


Figure 6. Longitude-vertical cross-sections of AIRS 3-D retrieved temperature perturbations. To suppress noise and clarify the westward-propagating GWs with horizontal wavelengths of ~400–650 km, a low-pass filter with a longitudinal cutoff wavelength of 3° (~230 km) was applied.

In summary, AIRS captured semi-concentric GWs with horizontal wavelengths of ~400–650 km and vertical wavelengths of ~25–30 km over the Korean Peninsula, northeastern China, Khabarovsk Krai in Russia, and Japan at ~05 and ~18 UT. Their phase structures indicate westward and upward propagation. The apparent epicenters of these GWs were located near the region north of Hokkaido (~47°N, ~148°E) at ~05 UT and (~43°N, ~145°E) at ~18 UT, where Himawari-9 indicated possible deep convection. These GW characteristics were reproduced in the WRF simulation as well, although the simulated amplitudes became less distinct at ~18 UT, unlike the pronounced GWs observed by AIRS.

3.2.2 Mesospheric GWs in the OH airglow layer observed by AWE

During the interval between the AIRS overpasses at ~05 and ~18 UT, AWE also observed GWs in the OH airglow layer (~87 km) over the same region.

Figure 7 shows relative radiance perturbations of the $Q_1(1)$ emission line (Figure 7a) and temperature perturbations (Figure 7b) at 11:47 UT. Figure 7c shows the cloud-presence probability estimated using a machine-learning method provided by Utah State University. Semi-concentric GWs appeared in both the emission and temperature perturbations over northeastern China and Khabarovsk Krai ($\sim 43-50°$N, $\sim 126-138°$E). Although some portions of the wave pattern

https://doi.org/10.5194/egusphere-2026-6104
Preprint. Discussion started: 5 November 2026
© Author(s) 2026. CC BY 4.0 License.

overlapped regions with cloud-presence probabilities exceeding 50%, coherent phase lines extended into adjacent regions where the cloud-presence probability was low, including near (~48°N, ~131°E). The continuity of these phase lines into regions with low cloud-presence probability, together with their presence in both the $Q_1(1)$ radiance and temperature perturbations, supports their interpretation as GWs rather than cloud-reflection artifacts. Their apparent epicenter was also
300 located north of Hokkaido, close to the possible deep convection region, and the GWs appeared to propagate westward. These characteristics are consistent with the stratospheric GWs. Figure 8 shows 2-D Lomb-Scargle spectra of the relative radiance perturbations and temperature perturbations. Because the 2-D spectra have a 180° directional ambiguity, we interpret the dominant wavevectors as westward-propagating based on the semi-concentric morphology and the location of the apparent epicenter. Both spectra roughly exhibit two large power areas around ($\sim -1.3 \times 10^{-3}$, ~0) cycle km^{-1},
305 corresponding to ~750 km, and (~ -2.5–-2.7×10^{-3}, ~0.0–-1.2×10^{-3}) cycle km^{-1}, corresponding to 300–400 km. Wave structures with horizontal wavelengths of $\sim 300 - 400$ km are clearly visible in Figure 7, whereas structures with wavelengths longer than ~600 km are less distinct. The temperature spectrum additionally exhibits a local peak near ($\sim -0.7 \times 10^{-3}$, $\sim 1.6 \times 10^{-3}$) cycle km^{-1} that is not apparent in the Q1(1) radiance spectrum. This additional peak might be attributed to cloud contamination and is therefore not considered further in this study.

310

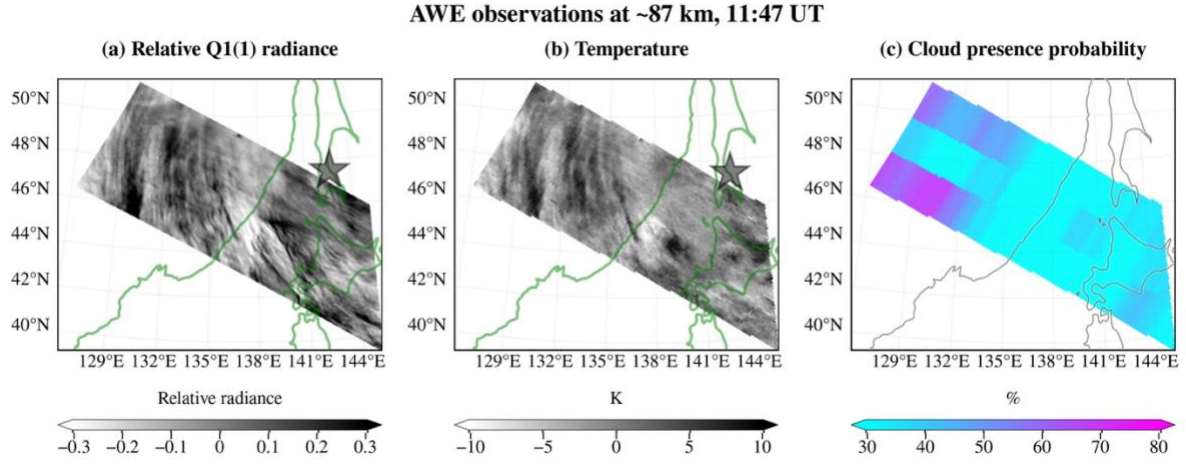


Figure 7. (a) Relative radiance perturbations of the $Q_1(1)$ emission line and (b) temperature perturbations at 11:47 UT. The stars indicate the GW apparent epicenter. (c) Cloud-presence probability estimated using a machine-learning method provided by Utah State University.

https://doi.org/10.5194/egusphere-2026-6104
Preprint. Discussion started: 5 November 2026
© Author(s) 2026. CC BY 4.0 License.

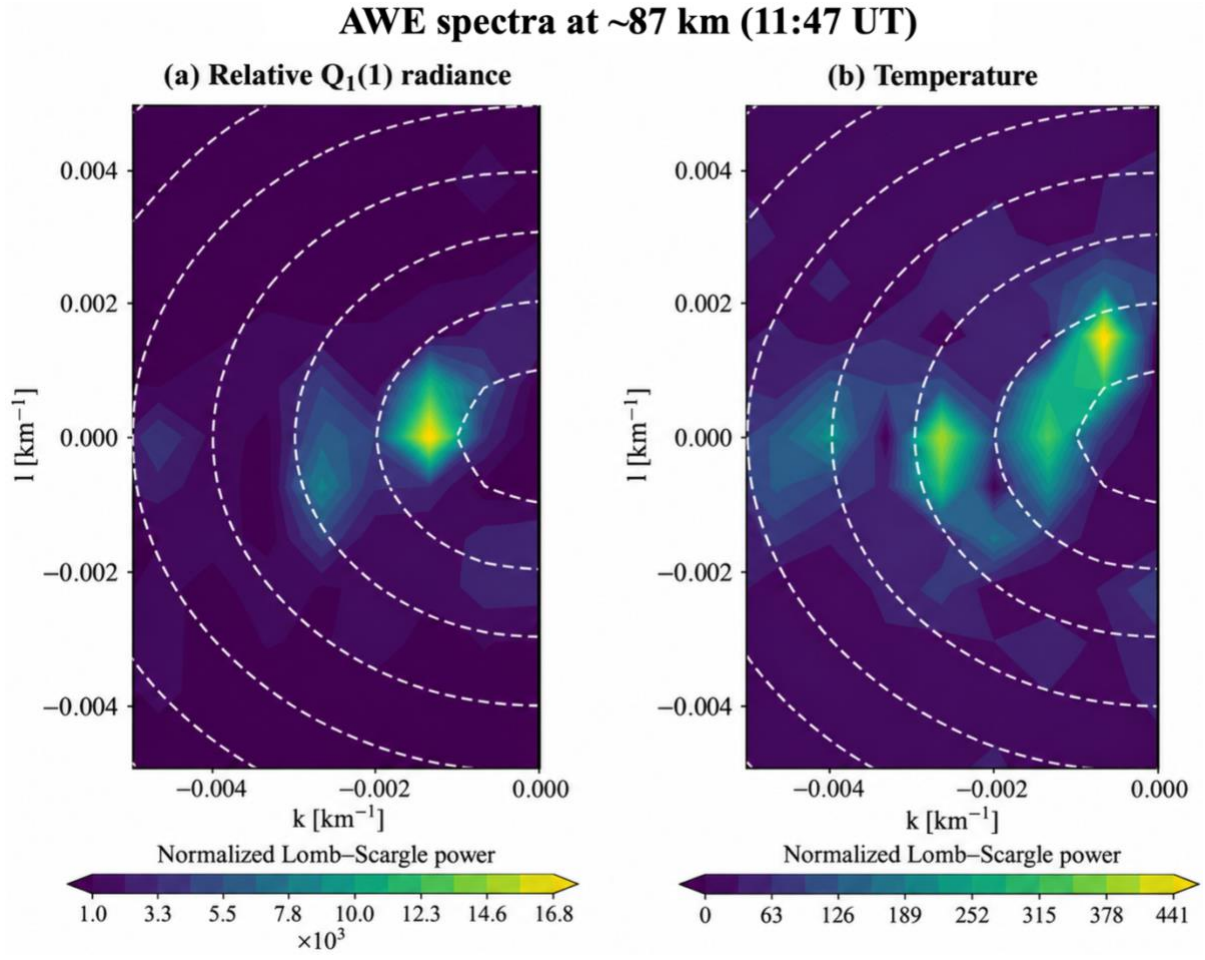


Figure 8. 2-D Lomb-Scargle power spectra for relative radiance perturbations of the $Q_1(1)$ emission line (a) and the temperature perturbations (b) at 11:47 UT. White dashed lines denote 0.001 [km^{-1}] intervals.

AWE also captured semi-concentric GWs over the Korean Peninsula and the Pacific Ocean during the next orbit at 13:20 UT (Figure 9). The semi-concentric GWs appeared to expand outward from northern Tohoku (~140°E, ~39°N), close to the possible region of deep convection identified by Himawari-9 (see Figure 1). The semi-concentric morphology is consistent with waves extending westward toward the Korean Peninsula, toward southwestern Japan, and southward over the Pacific Ocean. To minimize potential cloud contamination, we therefore restricted the spectral analysis to the Korean Peninsula in Figures 10(a,b), where the cloud-presence probability was relatively low (Figure 10c). The spectra of both the relative $Q_1(1)$ radiance and temperature perturbations showed a large value around ($\sim -2.4 \times 10^{-3}$, $\sim -1.0 – +0.3 \times 10^{-3}$) cycle km^{-1} in Figure 11. It should be noted that we assume westward propagation based on the observed morphology. Table 2 summarizes the local peaks of each spectrum.

https://doi.org/10.5194/egusphere-2026-6104
Preprint. Discussion started: 5 November 2026
© Author(s) 2026. CC BY 4.0 License.

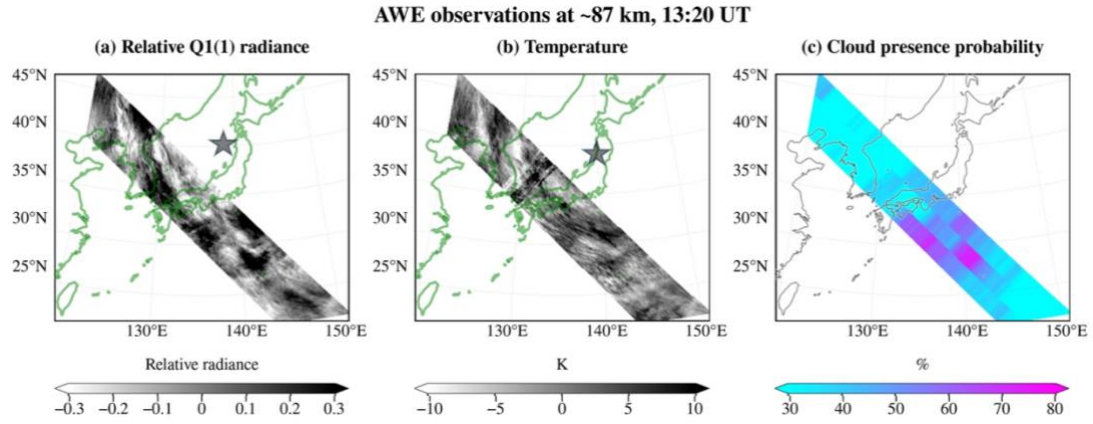


Figure 9. (a) Relative radiance perturbations of the $Q_1(1)$ emission line and (b) temperature perturbations at ~13 UT. The stars denote the GW apparent epicenter. (c) Cloud-presence probability estimated using a machine-learning method provided by Utah State University.

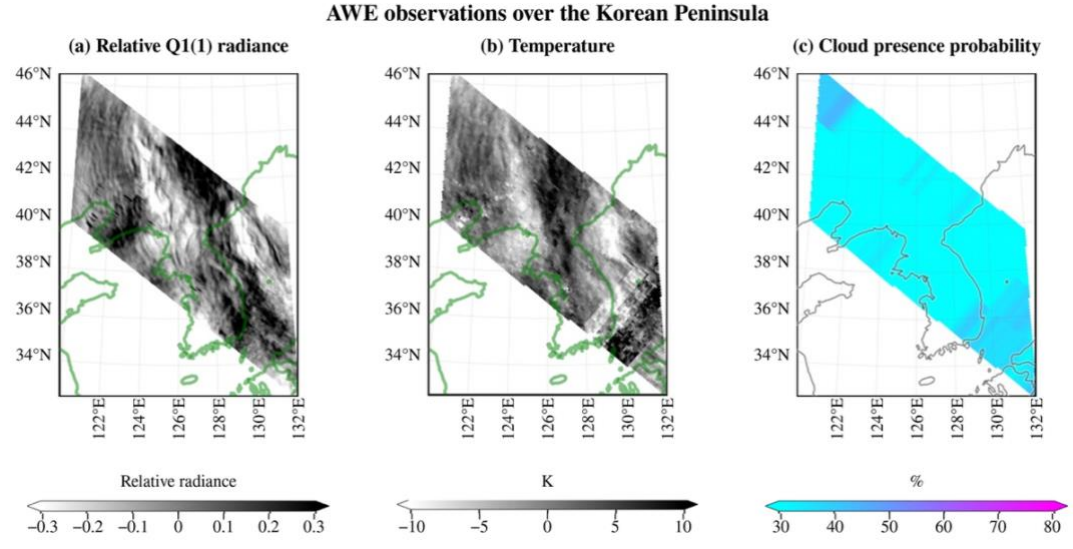


Figure 10. Same as Figure 9, but enlarged over the Korean Peninsula.

https://doi.org/10.5194/egusphere-2026-6104
Preprint. Discussion started: 5 November 2026
© Author(s) 2026. CC BY 4.0 License.

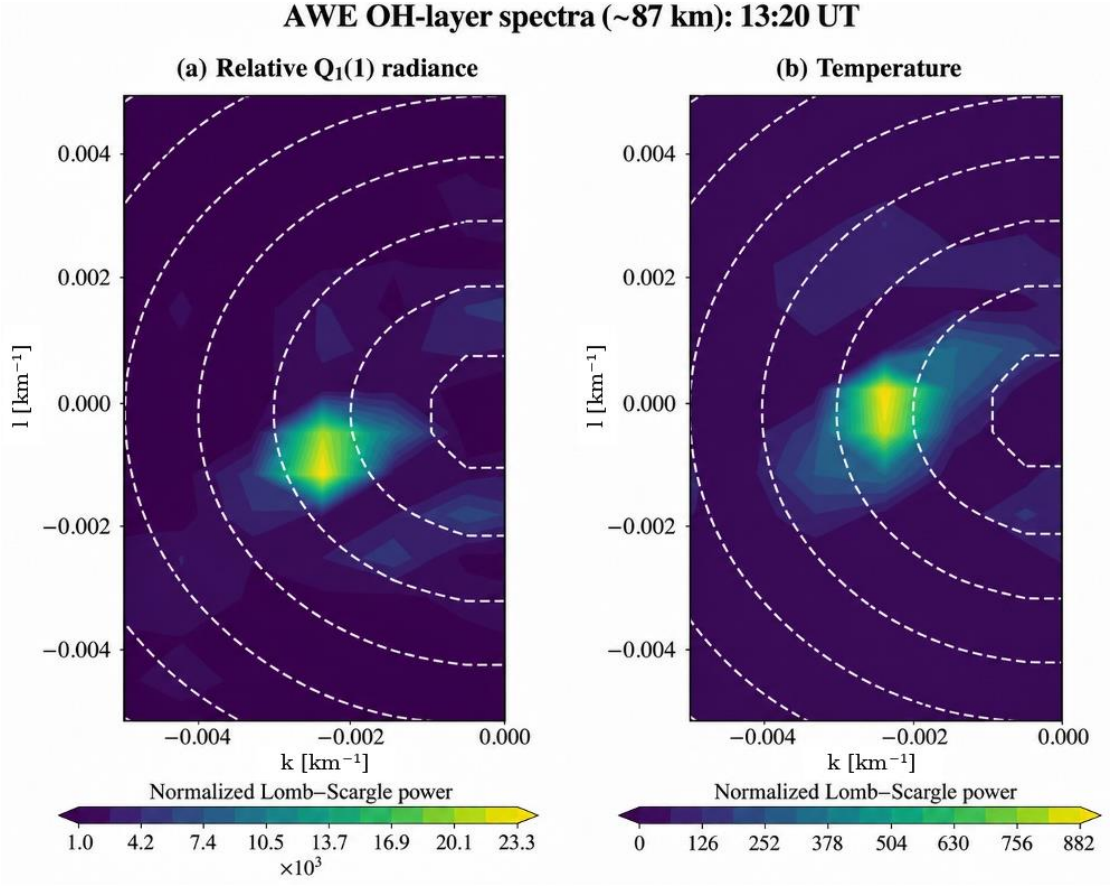


Figure 11. The same as Figure 8, but at 13:20 UT. White dashed lines denote 0.001 [km^{-1}] intervals.

335

Time	11:47				13:20			
	1st peak ($Q_1(1)$ line)	2nd peak ($Q_1(1)$ line)	1st peak (Temperature)	2nd peak (Temperature)	1st peak ($Q_1(1)$ line)	2nd peak ($Q_1(1)$ line)	1st peak (Temperature)	2nd peak (Temperature)
Azimuth angle [°]	270 (251–306)	244 (240–287)	270 (252–287)	270 (257–283)	248 (211–262)	262 (249–277)	278 (264–292)	262 (249–277)
Horizontal wavelength [km]	748 (556–1113)	360 (319–460)	751 (549–906)	376 (320–457)	394 (334–487)	423 (354–516)	420 (352–526)	420 (352–526)

Table 2. 1st and 2nd peaks of the Lomb-Scargle spectra in AWE. Values in parentheses indicate the parameter ranges corresponding to the full width at half maximum of each spectral peak. Azimuth angles are measured clockwise from north.

https://doi.org/10.5194/egusphere-2026-6104
Preprint. Discussion started: 5 November 2026
© Author(s) 2026. CC BY 4.0 License.

In summary, AWE observed semi-concentric GWs in both Q1(1) radiance and temperature perturbations at ~12 and ~13 UT. At ~12 UT, the two quantities exhibited consistent spectral peaks at horizontal wavelengths of ~750 and ~370 km, although GWs with horizontal wavelengths of ~750 km were invisible in the perturbations. At ~13 UT, the dominant wavelengths over the Korean Peninsula were ~390–420 km. The semi-concentric morphology and spectral orientations were generally consistent with a substantial westward component. These horizontal scales and morphology are consistent with those of the stratospheric GWs observed by AIRS before and after the AWE observations. The apparent epicenter of the GWs at ~12 UT was located north of Hokkaido, consistent with the apparent epicenter of the GWs observed by AIRS, whereas that at ~13 UT was located near northern Tohoku.

3.3 Propagation paths of the observed GWs and their potential sources

This section assesses the propagation paths of the observed GWs with the ray-tracing method and investigates their potential sources by combining the observations and WRF simulation. Although Section 3.2 shows the two stratospheric GW packets and the two mesospheric GW packets, this section focuses on the stratospheric GW packet at ~05 UT and the mesospheric GW packet at ~12 UT because their propagation paths and source regions are more clearly constrained than those of the other two packets. The ray-tracing method indicated that these two focused GW packets could have propagated directly from the vicinity of the possible deep convection region, i.e., north of Hokkaido (~47°N, 140–150°E). As for the remaining stratospheric GW packet at ~18 UT, the ray-tracing method indicates that it could also have been generated by deep convection (not shown), although the WRF simulation poorly reproduced both the GWs and convection. The remaining mesospheric GW packet at ~13 UT may also have been generated by deep convection, although its inferred source has greater uncertainty (not shown).

3.3.1 Backward propagation paths of the stratospheric GWs observed by AIRS and their potential sources

Figure 12 shows the ray paths of the GWs observed by AIRS at ~05 UT. The initial horizontal wavelengths were set to the 1st spectral peak obtained from the Lomb-Scargle analysis (see Table 1 and Figure 4a), and the background conditions were sampled along these paths. The initial vertical wavelength was set to 25 km based on their vertical structures in Figure 6a. The initial height was assumed to be 35 km, corresponding to the peak altitude of the AIRS kernel, and the initial horizontal locations were set at six points: (135°E, 44, 46, 48°N) and (138°E, 44, 46, 48°N), where the GW amplitude peaked in Figure 3a. The corresponding results using the second spectral peak from the Lomb-Scargle analysis are shown in Figure A2 in the Appendix and are very similar to those obtained using the first spectral peak. The backward rays reached the lower troposphere within $(139-143°\mathrm{E}, 45-49°\mathrm{N})$, suggesting this region as a possible source area, although it is longitudinally displaced from the apparent epicenter by $5-9°$. This discrepancy may be attributed to background-wind effects, whereby the semi-concentric structures were swept eastward by the background stratospheric winds (Vadas et al., 2009). Alternatively, it may

https://doi.org/10.5194/egusphere-2026-6104
Preprint. Discussion started: 5 November 2026
© Author(s) 2026. CC BY 4.0 License.

be due to uncertainties in the ray-tracing method associated with the initial location, spectral parameters, and background atmospheric conditions.

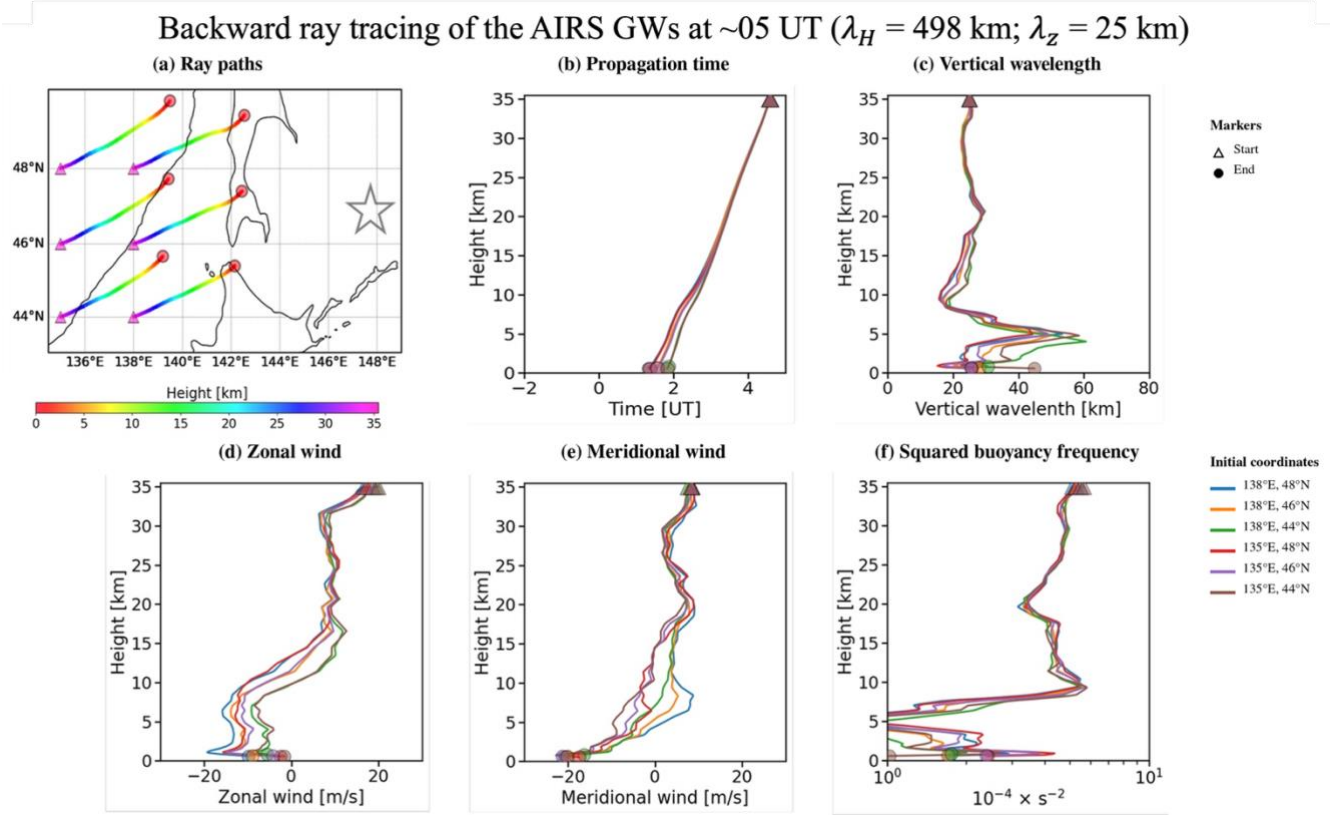


Figure 12. Backward ray paths of the GWs observed by AIRS at ~05 UT. (a) Backward ray paths. Colors represent height. (b) Propagation time. (c) Vertical wavelength. (d) Zonal wind. (e) Meridional wind. (f) Squared buoyancy frequency. Triangles and circles denote start and end points, respectively. The line colors in (b-f) correspond to the start points.

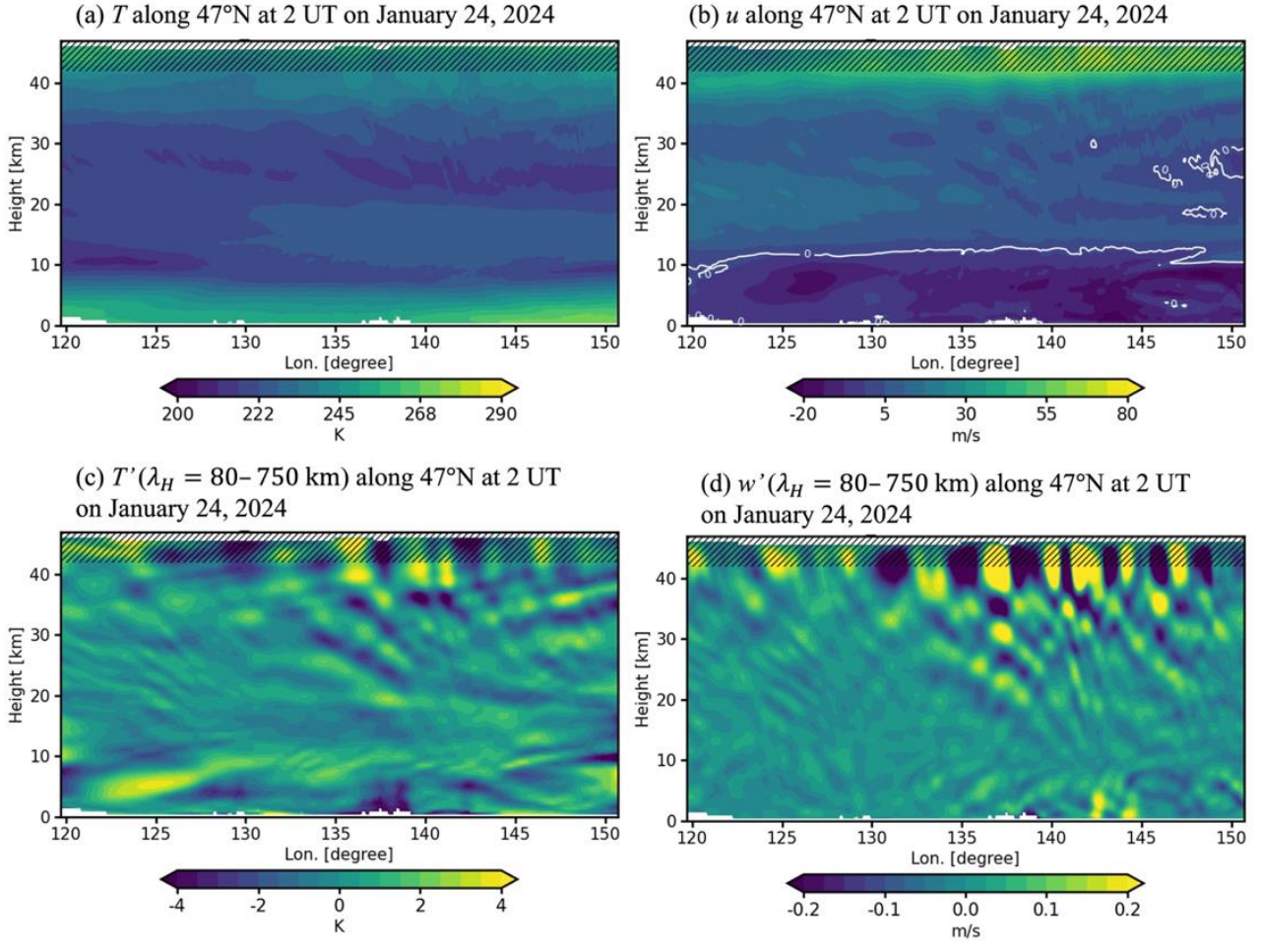
Because the ray-tracing results suggest that the stratospheric GWs were generated after ~01 UT (see Figure 12b), we investigated temperature and vertical-wind perturbations between 01 and 03 UT in the WRF simulation north of Hokkaido. Figure 13 shows a longitude-height cross-section of GW temperature (Figure 13c) and GW vertical-wind perturbations (Figure 13d) with horizontal wavelengths of 80–750 km along 47°N at 02 UT in the WRF simulation. Positive vertical-wind perturbations in the troposphere, indicative of convection, were enhanced around $(142 - 145°\text{E})$, overlapping the source region inferred from the backward ray analysis and the potential deep convection region identified by Himawari-9 (see Figure 1a). Coherent phase lines extended upward and westward from the convection at $(142 - 145°\text{E})$. Enhanced temperature perturbations were also seen around $(\sim 130 - 145°\text{E},\ \sim 20 - 40$ km), corresponding to both the region of enhanced vertical-wind perturbations in the WRF simulation and the region of enhanced GW temperature perturbations observed by AIRS (Figure 3a), although the phase lines of the temperature perturbations were unclear below ~20 km. Interestingly, a frontal

https://doi.org/10.5194/egusphere-2026-6104
Preprint. Discussion started: 5 November 2026
© Author(s) 2026. CC BY 4.0 License.

structure was also evident around (141 − 147°E), where convection was enhanced. The location of this front is consistent with that in Figure 2a. These features appeared continuously between ~00 and ~12 UT (see Movie 3 and Movie 4 in the supplement). Therefore, the GWs observed by AIRS at ~05 UT were most likely generated by deep convection within the cold front north of Hokkaido.

Although the apparent epicenter, ray-traced source region, and simulated convective source do not coincide pointwise, they are regionally consistent in locating the GW source north of Hokkaido, where Himawari-9 suggested that deep convection may have occurred. We interpret this regional agreement, rather than exact spatial coincidence, as evidence supporting a common convective source.

Vertical–longitude cross-sections along 47°N at 02:00 UT on 24 January 2024 from the WRF simulation



https://doi.org/10.5194/egusphere-2026-6104
Preprint. Discussion started: 5 November 2026
© Author(s) 2026. CC BY 4.0 License.

Figure 13. Longitude-height cross-section of the temperature (a), zonal wind (b), GW temperature perturbations, (c), and GW vertical wind perturbations (d), respectively, along 47°N at 02 UT in the WRF simulation. The white lines in (b) denote 0 m s^{-1}. Shaded areas denote the sponge layers

3.3.2 Forward propagation paths of the stratospheric GWs observed by AIRS and their breaking location

To investigate the potential saturation and breaking altitudes of the stratospheric GWs observed at ~05 UT, we conducted forward ray-tracing (Figure 14). The initial input amplitude was ~13 K, which was estimated from the observed amplitude (~0.5 K) divided by the response rate (~4%) for $\lambda_z = 25$ km. The forward ray-tracing results suggest that the GW packet propagated west-southwestward and, above an altitude of ~68 km, satisfied the criteria for both shear and convective instability, as its vertical wavelength decreased with decreasing background zonal wind at that altitude over Primorsky Krai, Russia (~133–136°E, 43–47°N), at ~06 UT. The GW packet then propagated a few degrees further westward, reached ~87 km, corresponding to the OH layer, at ~07 UT, and encountered its critical level at ~92 km at ~08 UT near the border between China and Russia (~130–133°E, 42–46°N). Thus, these stratospheric GWs could have passed through the OH layer at ~07 UT after becoming saturated, although AWE did not pass over this region at that time. This forward ray-tracing is not intended to demonstrate that the AIRS-observed packet corresponds to the GWs subsequently observed by AWE, but rather to assess whether GWs with the observed wave characteristics could reach the OH layer altitude during this winter storm. Furthermore, the predicted instability above ~68 km suggests that secondary GW generation below the OH layer cannot be excluded.

https://doi.org/10.5194/egusphere-2026-6104
Preprint. Discussion started: 5 November 2026
© Author(s) 2026. CC BY 4.0 License.

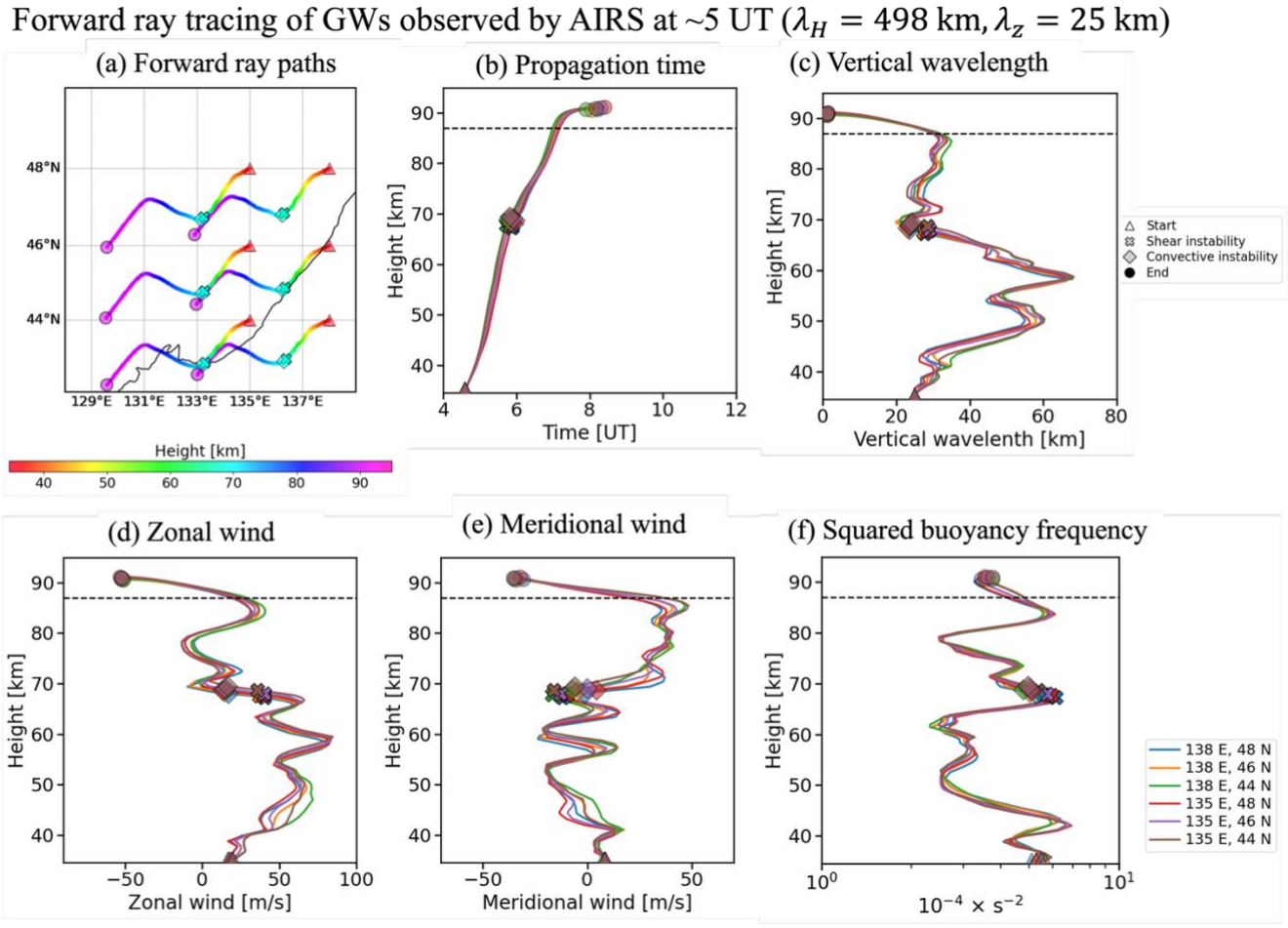


Figure 14. Forward ray paths of the GWs observed by AIRS at ~05 UT. (a) Forward ray paths. Colors represent height. (b) Propagation time. (c) Vertical wavelength. (d) Zonal wind. (e) Meridional wind. (f) Squared buoyancy frequency. Triangles and circles denote start and end points, respectively. Crosses and diamonds denote the lowest altitudes where GWs potentially met shear and convective instabilities, respectively. The line colors in (b-f) correspond to the start points.

3.3.3 Propagation paths of the mesospheric GWs observed by AWE and their potential sources

We also conducted backward ray tracing for the mesospheric GWs observed by AWE at ~12 UT. The initial positions were set at four locations: (131°E, 49°N), (132°E, 45°N), (134°E, 49°N), and (135°E, 45°N), with an altitude of 87 km. Because AWE does not provide direct information on vertical wavelengths but is sensitive primarily to GWs with vertical wavelengths longer than ~10 km, we tested vertical wavelengths of 10, 20, and 30 km. Figure 15 shows one example for GWs with $\lambda_H = 360$ km, corresponding to the second spectral peak in the Q1(1) radiance, and $\lambda_z = 10$ km. Because GWs with $\lambda_H = 360$ km are clearly visible in Figure 7, we focus on this case here. Results for the other parameters, including the first spectral peak ($\lambda_H = 748$ km), are shown in Figure A3 in the Appendix. The ray-tracing results in Figure

https://doi.org/10.5194/egusphere-2026-6104
Preprint. Discussion started: 5 November 2026
© Author(s) 2026. CC BY 4.0 License.

15 suggest that the GWs could have originated in the troposphere at (~138 − 143°E, ~49 − 53°N,) if they were generated in the troposphere. In particular, rays initialized at (135°E, 45°N) reached locations near the apparent epicenter (~142°E, ~48°N) at ~07 UT, in the broader region north of Hokkaido where Himawari-9 (Figure 1) and WRF indicated convection (Figure 13 and movies 3 and 4). GWs with the other parameter combinations could also have propagated from the troposphere north of Hokkaido, although their termination points vary in (136 − 149°E, 44 − 53°N) with the initial parameters, and the termination times vary from ~2 to ~10 UT (Figure A3). Therefore, like the stratospheric GWs, the mesospheric GWs were likely generated by deep convection within the front and could have propagated directly from the troposphere to the OH airglow layer. However, we cannot exclude the possibility of the secondary GW mechanism. The GWs observed by AWE likely propagated at ~70–80 km around (~135 − 139°E, ~47 − 51°N) at ~09–10 UT, while the forward ray tracing in Section 3.3.2 suggested that the observed stratospheric GWs were saturated at altitudes of ~70–80 km around (~133 − 137°E, ~43 − 47°N) at ~06–07 UT (compare Figures 14 and 15); that is, the two propagation paths overlapped at altitudes of ~70–80 km near (~135 − 137°E, ~47°N). Although their passage through this region was separated by ~2 hours, GW saturation may have occurred repeatedly because the WRF simulation indicated that GWs were continuously emitted by deep convection and propagated into the stratosphere.

https://doi.org/10.5194/egusphere-2026-6104
Preprint. Discussion started: 5 November 2026
© Author(s) 2026. CC BY 4.0 License.

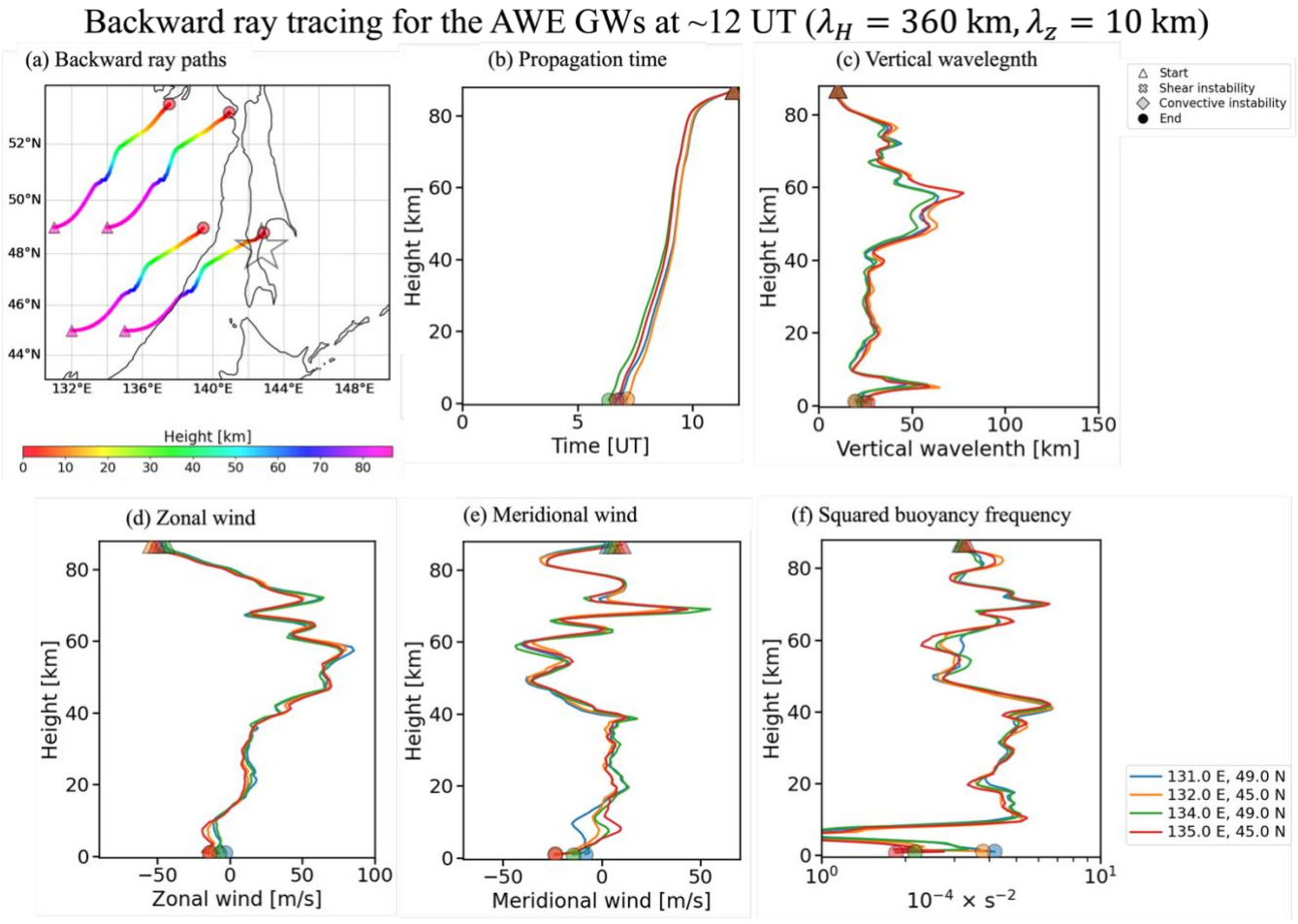


Figure 15. Backward ray paths of the GWs observed by AWE at ~12 UT. (a) Backward ray paths. Colors represent height. The star denotes the GW apparent epicenter. (b) Propagation time. (c) Vertical wavelength. (d) Zonal wind along the ray path. (e) Meridional wind. (f) Squared buoyancy frequency. Triangles and circles denote start and end points, respectively. The line colors in (b-f) correspond to the start points.

4 Discussion

The results presented in Section 3 indicate that the stratospheric GWs were most likely generated by deep convection within the cold front. The backward ray tracing also suggested that the mesospheric GWs could have originated from the same deep convection region and propagated directly to the OH layer altitude. The GWs were likely saturated above ~68 km and created local body force, which generated semi-concentric secondary GWs, during their upward propagation. Vadas and Azeem (2021) and Kogure et al. (2026) cautioned that concentric GWs in the mesosphere and thermosphere in the vicinity of deep convection can be misidentified as primary GWs directly generated by the convection. In those studies, turning levels of

https://doi.org/10.5194/egusphere-2026-6104
Preprint. Discussion started: 5 November 2026
© Author(s) 2026. CC BY 4.0 License.

the observed GWs were identified in the mesosphere or lower thermosphere and provided evidence supporting a secondary-GW interpretation. In the present winter-storm event, however, we did not identify a turning level for the mesospheric GWs observed by AWE. It should be noted that the absence of an identified turning level does not rule out secondary GW generation. Heale et al. (2022) simulated primary convectively generated GWs and secondary GWs with an idealized numerical model. In their simulation, primary GWs broke over the altitude range of 65–140 km, and both primary and secondary GWs coexisted above that wave-breaking altitude. Heale et al. (2022) noted that clearly separating primary from secondary GWs was difficult even in their relatively idealized simulation. Therefore, we do not further attempt to determine whether the mesospheric GWs observed by AWE were primary GWs, secondary GWs, or a superposition of both. Nevertheless, the combined observational, modeling, and ray−tracing results suggest that the ultimate tropospheric source of the mesospheric wave activity was most likely deep convection within the cold front, irrespective of whether the mesospheric GWs observed by AWE were primary or secondary.

Finally, GW generation associated with fronts and extratropical cyclones is not limited to convection; other mechanisms include flow over orography (i.e., mountain wave generation) (Pulido et al., 2013; Menchaca and Durran, 2017; Kogure et al., 2020; Becker et al., 2025) and spontaneous adjustment (Plougonven and Zhang, 2014; Kogure et al., 2023). In the stratosphere, GWs generated by these two mechanisms may often be distinguishable from convectively generated GWs based on their horizontal morphology because they do not necessarily exhibit concentric wavefronts. However, these two types of GWs may become saturated or break at higher altitudes and subsequently induce a local body force, generating secondary GWs that can exhibit concentric wavefronts. It can be challenging to identify their original wave source. Therefore, both tropospheric convective activity and the morphology of stratospheric GWs should be examined to reduce the risk of misidentifying the original sources of mesospheric GWs associated with fronts and extratropical cyclones. It should be noted that the WRF simulation clearly indicated that the GWs during this winter storm were generated by deep convection within the cold front (see Figure 13), supporting convection as the most likely original source.

5 Conclusion

This study investigated GWs associated with convection during the East Asian winter storm of 24 January 2024. Himawari-9 observations indicated deep convection north of Hokkaido ($\sim 144-151°$E, $\sim 43-48°$N), and the convection-permitting WRF simulation reproduced convection within a cold front under low-CAPE conditions with strong wind shear typical of wintertime frontal convection. AIRS observed semi-concentric GWs with horizontal wavelengths of several hundred kilometers in the stratosphere at ~05 UT, and AWE observed GWs with similar horizontal scales in the mesosphere at ~12 UT. The WRF simulation reproduced stratospheric GWs similar to those observed by AIRS between 0 and 12 UT and linked their generation to deep convection within the cold front north of Hokkaido ($\sim 142-145°$E, ~47°N). The convective region identified by Himawari-9, the simulated GW source, and the source region inferred from backward ray tracing did not coincide pointwise but were regionally consistent, with all three located north of Hokkaido. Separately, forward ray tracing indicated that the stratospheric GWs observed by AIRS could have crossed the OH airglow layer at ~07 UT after possibly

https://doi.org/10.5194/egusphere-2026-6104
Preprint. Discussion started: 5 November 2026
© Author(s) 2026. CC BY 4.0 License.

becoming saturated above ~68 km, during a gap in AWE coverage over East Asia. Backward ray tracing of the mesospheric GW packet observed by AWE suggested that the GWs originated from the convective region north of Hokkaido (136 − 149°E, 44 − 53°N) at ~02–10 UT. Together, these results provide event-resolved evidence linking the stratospheric and mesospheric GWs to wintertime convection within the cold front.

Previous event-resolved observations of convection-generated mesospheric GWs have focused mainly on tropical and warm-season midlatitude convection. By comparison, evidence for wintertime midlatitude events has come largely from statistical observational studies showing enhanced GW activity over the storm-track regions (Ern et al., 2011; Song et al., 2021; Kogure et al., 2025b), and some of these studies suggested that the enhanced activity was attributable to convection within extratropical cyclones. However, statistical analyses cannot fully separate the contribution of convection from the contributions of other factors. The present results complement these statistical and climatological findings by providing event-resolved evidence that convection occurring within a midlatitude wintertime cold front can contribute to GW activity in the upper mesosphere. Several limitations of this work should be noted. The WRF simulation reproduced the GWs only up to ~47 km, and AIRS and AWE did not continuously observe their propagation between the stratosphere and mesosphere. The inferred source connection with the mesospheric GWs therefore depends partly on ray tracing and its assumptions regarding the background atmosphere. The ray tracing results varied with the initial wave parameters, with termination points differing by a few to several degrees. However, some of them reached close to the potential deep convection region, and all ray paths reached the troposphere. Although this paper cannot identify whether mesospheric GWs were primary, secondary GWs, or a superposition of both, their original sources in the troposphere were most likely deep convection.

Our results demonstrate the value of combining observations, convection-permitting simulations, and ray tracing to identify the sources and propagation paths of stratospheric and mesospheric GWs. More broadly, they suggest that wintertime frontal convection in extratropical storm-track regions can act as an original source of GWs reaching the upper mesosphere.

https://doi.org/10.5194/egusphere-2026-6104
Preprint. Discussion started: 5 November 2026
© Author(s) 2026. CC BY 4.0 License.

Appendix.

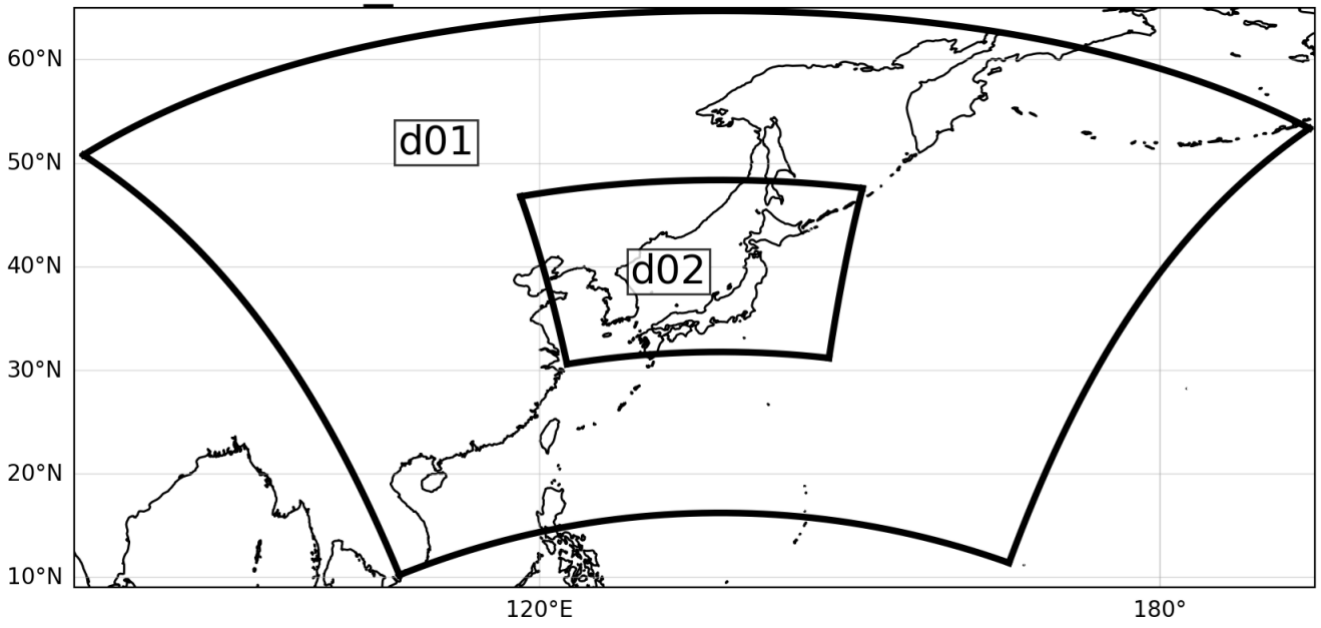


Figure A1. Domains 1 and 2 for the WRF simulation. They consisted of 800 × 600 and 802 × 601 grid points, with horizontal resolutions of 9 and 3 km, respectively.

https://doi.org/10.5194/egusphere-2026-6104
Preprint. Discussion started: 5 November 2026
© Author(s) 2026. CC BY 4.0 License.

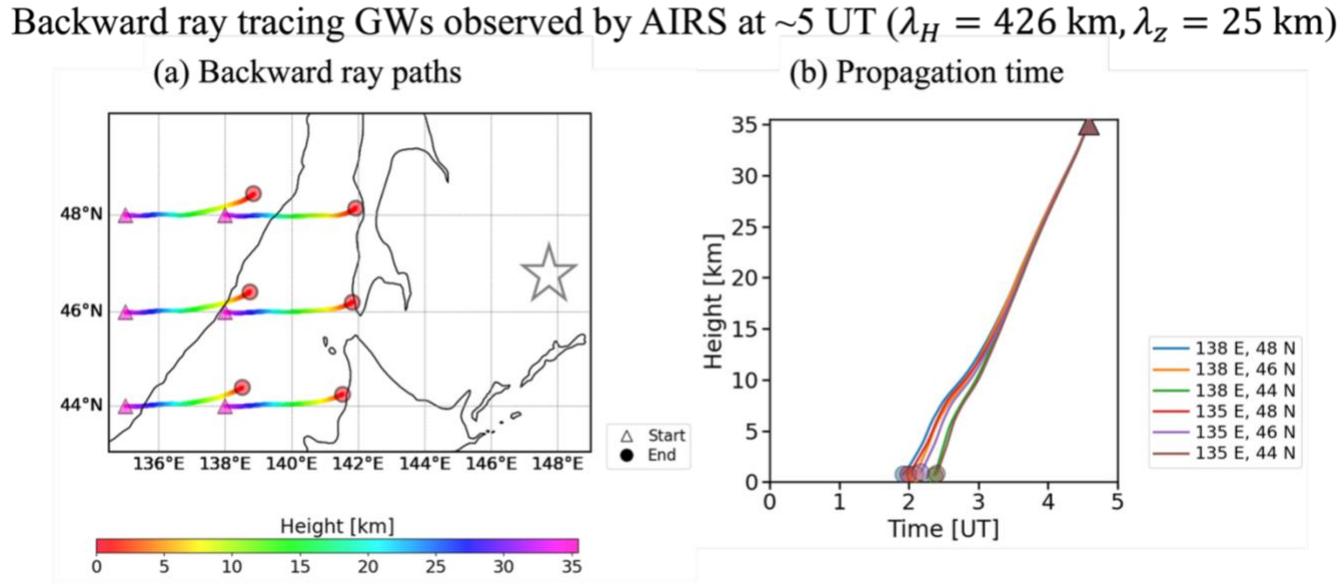


Figure A2. Backward ray paths of the GWs observed by AIRS at ~05 UT. (a) Backward ray paths. Colors represent height. (b) Propagation time. The line colors in (b) correspond to the start points. Triangles and circles denote start and end points, respectively.

https://doi.org/10.5194/egusphere-2026-6104
Preprint. Discussion started: 5 November 2026
© Author(s) 2026. CC BY 4.0 License.

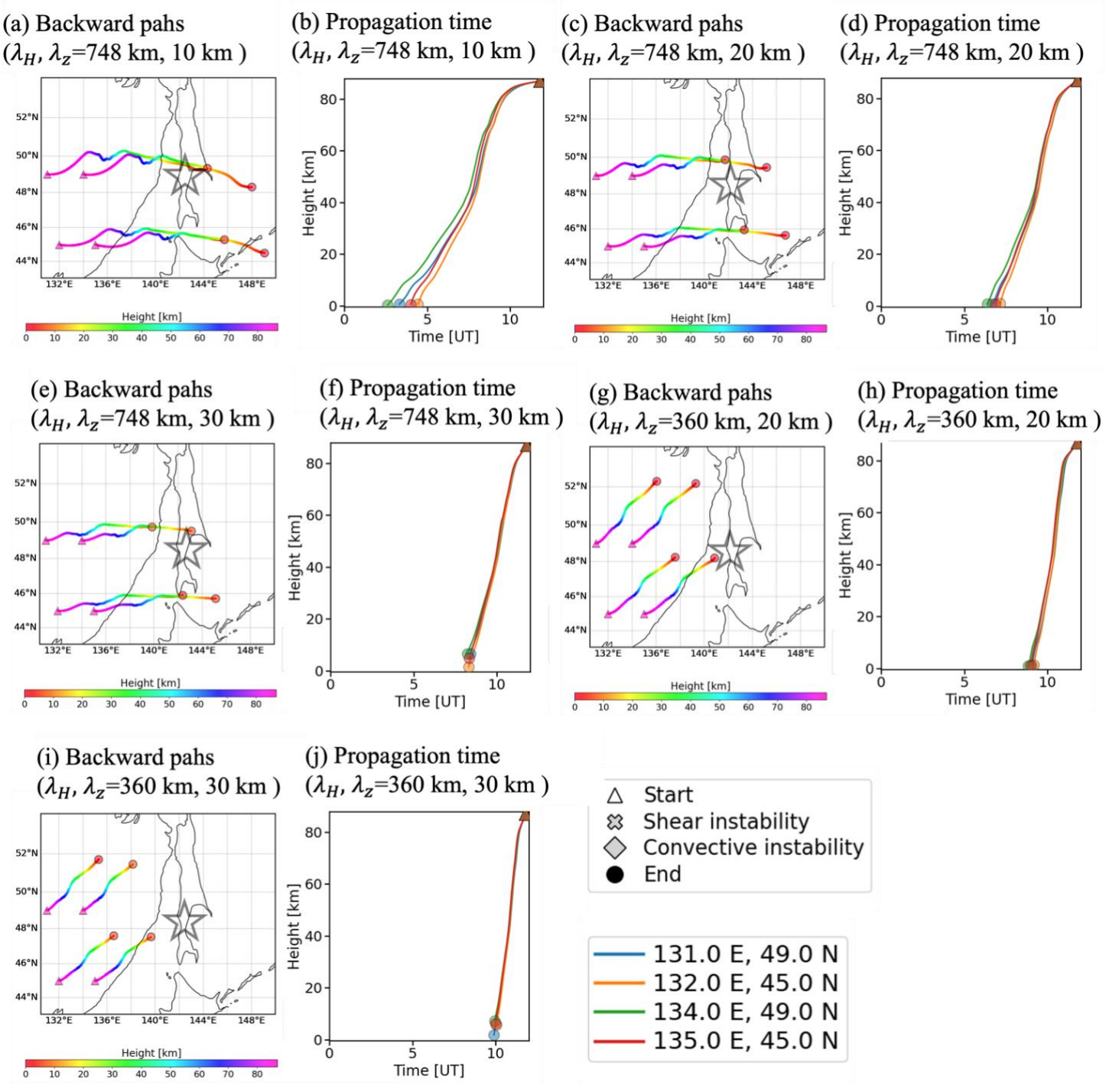


Figure A3. Backward ray paths of the GWs observed by AWE at ~12 UT. (a, c, e, g, i) Backward ray paths. Colors represent height. (b, d, f, h, j) Propagation time. The line colors correspond to the start points.

https://doi.org/10.5194/egusphere-2026-6104
Preprint. Discussion started: 5 November 2026
© Author(s) 2026. CC BY 4.0 License.

Code and data availability

AIRS data are provided by Forschungszentrum Jülich (Hoffmann, 2021): https://datapub.fz-juelich.de/slcs/airs/gravity_waves/index.html. JAWARA data are provided by the University of Tokyo (Sato and Koshin, 2025; Koshin et al., 2025): https://jawara.nipr.ac.jp/home. Our ray-tracing Python code (Kogure, 2025a) can be accessed via the following GitHub repository: https://github.com/masaru-kogure/raytracing. AWE data are provided by Utah State University (Scherliess, 2025): https://awe.physics.usu.edu/data/download/. The WRF model code is provided by Skamarock et al. (2019): https://github.com/wrf-model/WRF.

Supplement link

The supplementary movies are available from Zenodo at: https://doi.org/10.5281/zenodo.20745116.

Author contributions

MK conceptualized and designed the study, conducted the simulation, analyzed the data, and wrote the manuscript draft. All authors reviewed, edited, and contributed to the scientific discussion in the paper.

Competing interests

The contact author has declared that none of the authors has any competing interests.

Acknowledgements

This research was supported by Global – Learning & Academic research institution for Master's PhD students, and Postdocs (LAMP) Program of the National Research Foundation of Korea (NRF) grant funded by the Ministry of Education (no. RS-2024-00442483). This research was also supported by the Korea Astronomy and Space Science Institute under the R&D program (Project No. 2026183005) supervised by the Ministry of Science and ICT.

https://doi.org/10.5194/egusphere-2026-6104
Preprint. Discussion started: 5 November 2026
© Author(s) 2026. CC BY 4.0 License.



Financial support

This research has been supported by the National Research Foundation of Korea (grant no. RS-2024-00442483) and the Korea Astronomy and Space Science Institute under the R&D program (Project No. 2026183005) supervised by the Ministry of Science and ICT.

References

Aumann, H. H., Chahine, M. T., Gautier, C., Goldberg, M. D., Kalnay, E., McMillin, L. M., Revercomb, H., Rosenkranz, P. W., Smith, W. L., Staelin, D. H., Strow, L. L., and Susskind, J.: AIRS/AMSU/HSB on the Aqua mission: design, science objectives, data products, and processing systems, IEEE T. Geosci. Remote, 41, 253–264, https://doi.org/10.1109/TGRS.2002.808356, 2003.

Baker, D. J. and Stair Jr., A. T.: Rocket measurements of the altitude distributions of the hydroxyl airglow, Phys. Scripta, 37, 611–622, https://doi.org/10.1088/0031-8949/37/4/021, 1988.

Becker, E., Mrak, S., Vadas, S. L., and Huba, J. D.: Thermospheric gravity waves and ionospheric disturbances triggered by mountain waves over the western US in January 2017, J. Geophys. Res.-Space Phys., 130, e2025JA033951, https://doi.org/10.1029/2025JA033951, 2025.

Bessho, K., Date, K., Hayashi, M., Ikeda, A., Imai, T., Inoue, H., Kumagai, Y., Miyakawa, T., Murata, H., Ohno, T., Okuyama, A., Oyama, R., Sasaki, Y., Shimazu, Y., Shimoji, K., Sumida, Y., Suzuki, M., Taniguchi, H., Tsuchiyama, H., Uesawa, D., Yokota, H., and Yoshida, R.: An introduction to Himawari-8/9 – Japan's new-generation geostationary meteorological satellites, J. Meteorol. Soc. Jpn., 94, 151–183, https://doi.org/10.2151/jmsj.2016-009, 2016.

Bryan, G. H., Wyngaard, J. C., and Fritsch, J. M.: Resolution requirements for the simulation of deep moist convection, Mon. Weather Rev., 131, 2394–2416, https://doi.org/10.1175/1520-0493(2003)131<2394:RRFTSO>2.0.CO;2, 2003.

Burke, P. C. and Schultz, D. M.: A 4-year climatology of cold-season bow echoes over the continental United States, Weather Forecast., 19, 1061–1074, https://doi.org/10.1175/811.1, 2004.

Butchart, N., Charlton-Perez, A. J., Cionni, I., Hardiman, S. C., Haynes, P. H., Krüger, K., Kushner, P. J., Newman, P. A., Osprey, S. M., Perlwitz, J., Sigmond, M., Wang, L., Akiyoshi, H., Austin, J., Bekki, S., Baumgaertner, A., Braesicke, P., Brühl, C., Chipperfield, M., Dameris, M., Dhomse, S., Eyring, V., Garcia, R., Garny, H., Jöckel, P., Lamarque, J.-F., Marchand, M., Michou, M., Morgenstern, O., Nakamura, T., Pawson, S., Plummer, D., Pyle, J., Rozanov, E., Scinocca, J., Shepherd, T. G., Shibata, K., Smale, D., Teyssèdre, H., Tian, W., Waugh, D., and Yamashita, Y.: Multimodel climate and variability of the stratosphere, J. Geophys. Res.-Atmos., 116, D05102, https://doi.org/10.1029/2010JD014995, 2011.

Cao, B. and Liu, A. Z.: Statistical characteristics of high-frequency gravity waves observed by an airglow imager at Andes Lidar Observatory, Earth Space Sci., 9, e2022EA002256, https://doi.org/10.1029/2022EA002256, 2022.

Celiński-Mysław, D. and Matuszko, D.: An analysis of selected cases of derecho in Poland, Atmos. Res., 149, 263–281, https://doi.org/10.1016/j.atmosres.2014.06.016, 2014.

Celiński-Mysław, D., Palarz, A., and Taszarek, M.: Climatology and atmospheric conditions associated with cool-season bow echo storms in Poland, Atmos. Res., 240, 104944, https://doi.org/10.1016/j.atmosres.2020.104944, 2020.

Chahine, M. T., Pagano, T. S., Aumann, H. H., Atlas, R., Barnet, C., Blaisdell, J., Chen, L., Divakarla, M., Fetzer, E. J., Goldberg, M., Gautier, C., Granger, S., Hannon, S., Irion, F. W., Kakar, R., Kalnay, E., Lambrigtsen, B. H., Lee, S.-Y., Le Marshall, J., McMillan, W. W., McMillin, L., Olsen, E. T., Revercomb, H., Rosenkranz, P., Smith, W. L.,

https://doi.org/10.5194/egusphere-2026-6104
Preprint. Discussion started: 5 November 2026
© Author(s) 2026. CC BY 4.0 License.

Staelin, D., Strow, L. L., Susskind, J., Tobin, D., Wolf, W., and Zhou, L.: AIRS: improving weather forecasting and providing new data on greenhouse gases, Bull. Amer. Meteor. Soc., 87, 911–926, https://doi.org/10.1175/BAMS-87-7-911, 2006.

Choi, H.-J. and Chun, H.-Y.: Momentum flux spectrum of convective gravity waves. Part I: An update of a parameterization using mesoscale simulations, J. Atmos. Sci., 68, 739–759, https://doi.org/10.1175/2010JAS3552.1, 2011.

Choi, H.-J. and Chun, H.-Y.: Effects of convective gravity wave drag in the Southern Hemisphere winter stratosphere, J. Atmos. Sci., 70, 2120–2136, https://doi.org/10.1175/JAS-D-12-0238.1, 2013.

Clark, M. R.: The southern England tornadoes of 30 December 2006: case study of a tornadic storm in a low-CAPE, high-shear environment, Atmos. Res., 93, 50–65, https://doi.org/10.1016/j.atmosres.2008.10.008, 2009.

Clark, M. R.: A provisional climatology of cool-season convective lines in the UK, Atmos. Res., 123, 180–196, https://doi.org/10.1016/j.atmosres.2012.09.018, 2013.

Clark, T. L., Hauf, T., and Kuettner, J. P.: Convectively forced internal gravity waves: results from two-dimensional numerical experiments, Q. J. Roy. Meteor. Soc., 112, 899–925, https://doi.org/10.1002/qj.49711247402, 1986.

de Orla-Barile, M., Cannon, F., Oakley, N. S., and Ralph, F. M.: A climatology of narrow cold-frontal rainbands in Southern California, Geophys. Res. Lett., 49, e2021GL095362, https://doi.org/10.1029/2021GL095362, 2022.

Ern, M., Preusse, P., Gille, J. C., Hepplewhite, C. L., Mlynczak, M. G., Russell III, J. M., and Riese, M.: Implications for atmospheric dynamics derived from global observations of gravity wave momentum flux in stratosphere and mesosphere, J. Geophys. Res., 116, D19107, https://doi.org/10.1029/2011JD015821, 2011.

Fovell, R., Durran, D., and Holton, J. R.: Numerical simulation of convectively generated stratospheric gravity waves, J. Atmos. Sci., 49, 1427–1442, https://doi.org/10.1175/1520-0469(1992)049<1427:NSOCGS>2.0.CO;2, 1992.

Fritts, D. C. and Alexander, M. J.: Gravity wave dynamics and effects in the middle atmosphere, Rev. Geophys., 41, 1003, https://doi.org/10.1029/2001RG000106, 2003.

Garcia, R. R., Smith, A. K., Kinnison, D. E., Murphy, D. J., and de la Cámara, Á.: Modification of the gravity wave parameterization in the Whole Atmosphere Community Climate Model: motivation and results, J. Atmos. Sci., 74, 275–291, https://doi.org/10.1175/JAS-D-16-0104.1, 2017.

Gatzen, C.: A 10-year climatology of cold-season narrow cold-frontal rainbands in Germany, Atmos. Res., 100, 366–370, https://doi.org/10.1016/j.atmosres.2010.09.018, 2011.

Geller, M. A. and Gong, J.: Gravity wave kinetic, potential, and vertical fluctuation energies as indicators of different frequency gravity waves, J. Geophys. Res., 115, D11111, https://doi.org/10.1029/2009JD012266, 2010.

Heale, C. J., Inchin, P. A., and Snively, J. B.: Primary versus secondary gravity wave responses at F-region heights generated by a convective source, J. Geophys. Res.-Space Phys., 127, e2021JA029947, https://doi.org/10.1029/2021JA029947, 2022.

Hersbach, H., Bell, B., Berrisford, P., Hirahara, S., Horányi, A., Muñoz-Sabater, J., Nicolas, J., Peubey, C., Radu, R., Schepers, D., Simmons, A., Soci, C., Abdalla, S., Abellan, X., Balsamo, G., Bechtold, P., Biavati, G., Bidlot, J., Bonavita, M., De Chiara, G., Dahlgren, P., Dee, D., Diamantakis, M., Dragani, R., Flemming, J., Forbes, R., Fuentes, M., Geer, A., Haimberger, L., Healy, S., Hogan, R. J., Hólm, E., Janisková, M., Keeley, S., Laloyaux, P., Lopez, P., Lupu, C., Radnoti, G., de Rosnay, P., Rozum, I., Vamborg, F., Villaume, S., and Thépaut, J.-N.: The ERA5 global reanalysis, Q. J. Roy. Meteor. Soc., 146, 1999–2049, https://doi.org/10.1002/qj.3803, 2020.

Hoffmann, L.: AIRS/Aqua observations of gravity waves, Jülich DATA [data set], https://doi.org/10.26165/JUELICH-DATA/LQAAJA, 2021.

https://doi.org/10.5194/egusphere-2026-6104
Preprint. Discussion started: 5 November 2026
© Author(s) 2026. CC BY 4.0 License.

Hoffmann, L. and Alexander, M. J.: Retrieval of stratospheric temperatures from Atmospheric Infrared Sounder radiance measurements for gravity wave studies, J. Geophys. Res., 114, D07105, https://doi.org/10.1029/2008JD011241, 2009.

Hoffmann, L., Xue, X., and Alexander, M. J.: A global view of stratospheric gravity wave hotspots located with Atmospheric Infrared Sounder observations, J. Geophys. Res.-Atmos., 118, 416–434, https://doi.org/10.1029/2012JD018658, 2013.

Hoffmann, L., Alexander, M. J., Clerbaux, C., Grimsdell, A. W., Meyer, C. I., Rößler, T., and Tournier, B.: Intercomparison of stratospheric gravity wave observations with AIRS and IASI, Atmos. Meas. Tech., 7, 4517–4537, https://doi.org/10.5194/amt-7-4517-2014, 2014.

Hoffmann, L., Grimsdell, A. W., and Alexander, M. J.: Stratospheric gravity waves at Southern Hemisphere orographic hotspots: 2003–2014 AIRS/Aqua observations, Atmos. Chem. Phys., 16, 9381–9397, https://doi.org/10.5194/acp-16-9381-2016, 2016.

Hoffmann, L., Spang, R., Orr, A., Alexander, M. J., Holt, L. A., and Stein, O.: A decadal satellite record of gravity wave activity in the lower stratosphere to study polar stratospheric cloud formation, Atmos. Chem. Phys., 17, 2901–2920, https://doi.org/10.5194/acp-17-2901-2017, 2017.

Holton, J. R.: The influence of gravity wave breaking on the general circulation of the middle atmosphere, J. Atmos. Sci., 40, 2497–2507, https://doi.org/10.1175/1520-0469(1983)040<2497:TIOGWB>2.0.CO;2, 1983.

Japan Meteorological Agency: Himawari-8/9 Himawari Standard Data User's Guide, Japan Meteorological Agency, Tokyo, Japan, available at: https://www.data.jma.go.jp/mscweb/en/support/support.html (last access: 18 June 2026), 2015.

Kang, M.-J., Chun, H.-Y., and Kim, Y.-H.: Momentum flux of convective gravity waves derived from an offline gravity wave parameterization. Part I: Spatiotemporal variations at source level, J. Atmos. Sci., 74, 3167–3189, https://doi.org/10.1175/JAS-D-17-0053.1, 2017.

King, J. R., Parker, M. D., Sherburn, K. D., and Lackmann, G. M.: Rapid evolution of cool-season, low-CAPE severe thunderstorm environments, Weather Forecast., 32, 763–779, https://doi.org/10.1175/WAF-D-16-0141.1, 2017.

Kogure, M.: Ray-tracing Python code, GitHub [code], available at: https://github.com/masaru-kogure/raytracing, https://doi.org/10.5281/zenodo.15572959, 2025a.

Kogure, M., Nakamura, T., Ejiri, M. K., Nishiyama, T., Tomikawa, Y., and Tsutsumi, M.: Effects of horizontal wind structure on a gravity wave event in the middle atmosphere over Syowa (69°S, 40°E), the Antarctic, Geophys. Res. Lett., 45, 5151–5157, https://doi.org/10.1029/2018GL078264, 2018.

Kogure, M., Yue, J., Nakamura, T., Hoffmann, L., Vadas, S. L., Tomikawa, Y., Ejiri, M. K., and Janches, D.: First direct observational evidence for secondary gravity waves generated by mountain waves over the Andes, Geophys. Res. Lett., 47, e2020GL088845, https://doi.org/10.1029/2020GL088845, 2020.

Kogure, M., Nakamura, T., Murphy, D. J., Taylor, M. J., Zhao, Y., Pautet, P.-D., Ejiri, M. K., Tsutsumi, M., Suzuki, H., Tomikawa, Y., and Nishiyama, T.: Characteristics of gravity wave horizontal phase velocity spectra in the mesosphere over the Antarctic stations, Syowa and Davis, J. Geophys. Res.-Atmos., 128, e2022JD037751, https://doi.org/10.1029/2022JD037751, 2023.

Kogure, M., Chou, M.-Y., Yue, J., Otsuka, Y., Liu, H., Sassi, F., Pedatella, N., Randall, C. E., and Harvey, V. L.: Medium-scale traveling ionospheric disturbances created by primary gravity waves generated by a winter storm, J. Space Weather Space Clim., 14, 38, https://doi.org/10.1051/swsc/2024036, 2024.

Kogure, M., Yue, J., Chou, M.-Y., Liu, H., Otsuka, Y., Randall, C. E., Hoffmann, L., and Hozumi, Y.: Coincident/simultaneous observations of stratospheric concentric gravity waves and concentric traveling ionospheric disturbances over the continental U.S. in 2022, J. Geophys. Res.-Space Phys., 130, e2024JA033429, https://doi.org/10.1029/2024JA033429, 2025b.

https://doi.org/10.5194/egusphere-2026-6104
Preprint. Discussion started: 5 November 2026
© Author(s) 2026. CC BY 4.0 License.



Kogure, M., Song, I.-S., Song, B.-G., Liu, H., Nishioka, M., Perwitasari, S., Kam, H., and Hong, J.: Medium-scale traveling ionospheric disturbances induced by secondary gravity waves associated with record-breaking heavy rainfall in August 2021 over Kyushu, Japan, J. Geophys. Res.-Space Phys., 131, e2025JA034997, https://doi.org/10.1029/2025JA034997, 2026.

Koshin, D., Sato, K., Watanabe, S., and Miyazaki, K.: The JAGUAR-DAS whole neutral atmosphere reanalysis: JAWARA, Prog. Earth Planet. Sci., 12, 1, https://doi.org/10.1186/s40645-024-00674-3, 2025.

Lamborn, B., Scherliess, L., Ruley, L., Latvakoski, H., Syrstad, E., Sevilla, P., Zhao, Y., Cantwell, G., Taylor, M., and Pautet, P.-D.: Atmospheric Waves Experiment (AWE) mission overview, Proc. SPIE, 13144, 131440Q, https://doi.org/10.1117/12.3027141, 2024.

Li, Q., Xu, J., Zhu, Y., Wrasse, C. M., Bageston, J. V., Yuan, W., Liu, X., Liu, W., Wen, Y., Li, H., and Liu, Z.: Extreme concentric gravity waves observed in the mesosphere and thermosphere regions over southern Brazil associated with fast-moving severe thunderstorms, Atmos. Chem. Phys., 25, 9719–9736, https://doi.org/10.5194/acp-25-9719-2025, 2025.

Lindzen, R. S.: Turbulence and stress owing to gravity wave and tidal breakdown, J. Geophys. Res., 86, 9707–9714, https://doi.org/10.1029/JC086iC10p09707, 1981.

Ludwig, P., Pinto, J. G., Hoepp, S. A., Fink, A. H., and Gray, S. L.: Secondary cyclogenesis along an occluded front leading to damaging wind gusts: windstorm Kyrill, January 2007, Mon. Weather Rev., 143, 1417–1437, https://doi.org/10.1175/MWR-D-14-00304.1, 2015.

Marks, C. J. and Eckermann, S. D.: A three-dimensional nonhydrostatic ray-tracing model for gravity waves: formulation and preliminary results for the middle atmosphere, J. Atmos. Sci., 52, 1959–1984, https://doi.org/10.1175/1520-0469(1995)052<1959:ATDNRT>2.0.CO;2, 1995.

Matsuno, T.: A quasi one-dimensional model of the middle atmosphere circulation interacting with internal gravity waves, J. Meteorol. Soc. Jpn., 60, 215–226, https://doi.org/10.2151/jmsj1965.60.1_215, 1982.

Mathias, L., Ermert, V., Kelemen, F. D., Ludwig, P., and Pinto, J. G.: Synoptic-scale conditions and convection-resolving hindcast experiments of a cold-season derecho on 3 January 2014 in western Europe, Nat. Hazards Earth Syst. Sci., 19, 1023–1040, https://doi.org/10.5194/nhess-19-1023-2019, 2019.

Menchaca, M. Q. and Durran, D. R.: Mountain waves, downslope winds, and low-level blocking forced by a midlatitude cyclone encountering an isolated ridge, J. Atmos. Sci., 74, 617–639, https://doi.org/10.1175/JAS-D-16-0092.1, 2017.

Nyassor, P. K., Wrasse, C. M., Gobbi, D., Paulino, I., Vadas, S. L., Naccarato, K. P., Takahashi, H., Bageston, J. V., Figueiredo, C. A. O. B., and Barros, D.: Case studies on concentric gravity waves source using lightning flash rate, brightness temperature and backward ray tracing at São Martinho da Serra (29.44°S, 53.82°W), J. Geophys. Res.-Atmos., 126, e2020JD034527, https://doi.org/10.1029/2020JD034527, 2021.

Nyassor, P. K., Wrasse, C. M., Paulino, I., São Sabbas, E. F. M. T., Bageston, J. V., Naccarato, K. P., Gobbi, D., Figueiredo, C. A. O. B., Ayorinde, T. T., Takahashi, H., and Barros, D.: Sources of concentric gravity waves generated by a moving mesoscale convective system in southern Brazil, Atmos. Chem. Phys., 22, 15153–15177, https://doi.org/10.5194/acp-22-15153-2022, 2022.

Pautet, P.-D., Taylor, M. J., Pendleton Jr., W. R., Zhao, Y., Yuan, T., Esplin, R., and McLain, D.: Advanced mesospheric temperature mapper for high-latitude airglow studies, Appl. Optics, 53, 5934–5943, https://doi.org/10.1364/AO.53.005934, 2014.

Piani, C., Durran, D., Alexander, M. J., and Holton, J. R.: A numerical study of three-dimensional gravity waves triggered by deep tropical convection and their role in the dynamics of the QBO, J. Atmos. Sci., 57, 3689–3702, https://doi.org/10.1175/1520-0469(2000)057<3689:ANSOTD>2.0.CO;2, 2000.

https://doi.org/10.5194/egusphere-2026-6104
Preprint. Discussion started: 5 November 2026
© Author(s) 2026. CC BY 4.0 License.

Plougonven, R. and Zhang, F.: Internal gravity waves from atmospheric jets and fronts, Rev. Geophys., 52, 33–76, https://doi.org/10.1002/2012RG000419, 2014.

Prein, A. F., Langhans, W., Fosser, G., Ferrone, A., Ban, N., Goergen, K., Keller, M., Tölle, M., Gutjahr, O., Feser, F., Brisson, E., Kollet, S., Schmidli, J., van Lipzig, N. P. M., and Leung, R.: A review on regional convection-permitting climate modeling: demonstrations, prospects, and challenges, Rev. Geophys., 53, 323–361, https://doi.org/10.1002/2014RG000475, 2015.

Pulido, M., Rodas, C., Dechat, D., and Lucini, M. M.: High gravity-wave activity observed in Patagonia, southern South America: generation by a cyclone passage over the Andes mountain range, Q. J. Roy. Meteor. Soc., 139, 451–466, https://doi.org/10.1002/qj.1983, 2013.

Púčik, T., Groenemeijer, P., Rýva, D., and Kolář, M.: Proximity soundings of severe and nonsevere thunderstorms in central Europe, Mon. Weather Rev., 143, 4805–4821, https://doi.org/10.1175/MWR-D-15-0104.1, 2015.

Sato, K. and Koshin, D.: JAGUAR Data Assimilation System Whole neutral Atmosphere Reanalysis (JAWARA), National Institute of Polar Research [data set], https://doi.org/10.17592/002.2025010407, 2025.

Scherliess, L.: AWE data, Utah State University [data set], available at: https://awe.physics.usu.edu/data/download/, 2025.

Sentman, D. D., Wescott, E. M., Picard, R. H., Winick, J. R., Stenbaek-Nielsen, H. C., Dewan, E. M., Moudry, D. R., São Sabbas, F. T., Heavner, M. J., and Morrill, J.: Simultaneous observations of mesospheric gravity waves and sprites generated by a midwestern thunderstorm, J. Atmos. Sol.-Terr. Phys., 65, 537–550, https://doi.org/10.1016/S1364-6826(02)00328-0, 2003.

Sherburn, K. D. and Parker, M. D.: Climatology and ingredients of significant severe convection in high-shear, low-CAPE environments, Weather Forecast., 29, 854–877, https://doi.org/10.1175/WAF-D-13-00041.1, 2014.

Sherburn, K. D., Parker, M. D., King, J. R., and Lackmann, G. M.: Composite environments of severe and nonsevere high-shear, low-CAPE convective events, Weather Forecast., 31, 1899–1927, https://doi.org/10.1175/WAF-D-16-0086.1, 2016.

Skamarock, W. C., Klemp, J. B., Dudhia, J., Gill, D. O., Liu, Z., Berner, J., Wang, W., Powers, J. G., Duda, M. G., Barker, D. M., and Huang, X.-Y.: A description of the Advanced Research WRF Model Version 4, NCAR Technical Note NCAR/TN-556+STR, https://doi.org/10.5065/1DFH-6P97, 2019.

Song, B.-G., Song, I.-S., Chun, H.-Y., Lee, C., Kam, H., Kim, Y. H., Kang, M.-J., Hindley, N. P., and Mitchell, N. J.: Activities of small-scale gravity waves in the upper mesosphere observed from meteor radar at King Sejong Station, Antarctica (62.22°S, 58.78°W), and their potential sources, J. Geophys. Res.-Atmos., 126, e2021JD034528, https://doi.org/10.1029/2021JD034528, 2021.

Song, I.-S. and Chun, H.-Y.: Momentum flux spectrum of convectively forced internal gravity waves and its application to gravity wave drag parameterization. Part I: theory, J. Atmos. Sci., 62, 107–124, https://doi.org/10.1175/JAS-3363.1, 2005.

Suzuki, S., Shiokawa, K., Otsuka, Y., Ogawa, T., Nakamura, K., and Nakamura, T.: A concentric gravity wave structure in the mesospheric airglow images, J. Geophys. Res., 112, D02102, https://doi.org/10.1029/2005JD006558, 2007.

Taylor, M. J. and Hapgood, M. A.: Identification of a thunderstorm as a source of short period gravity waves in the upper atmospheric nightglow emissions, Planet. Space Sci., 36, 975–985, https://doi.org/10.1016/0032-0633(88)90035-9, 1988.

Vadas, S. L. and Azeem, I.: Concentric secondary gravity waves in the thermosphere and ionosphere over the continental United States on March 25–26, 2015 from deep convection, J. Geophys. Res.-Space Phys., 126, e2020JA028275, https://doi.org/10.1029/2020JA028275, 2021.

https://doi.org/10.5194/egusphere-2026-6104
Preprint. Discussion started: 5 November 2026
© Author(s) 2026. CC BY 4.0 License.



Vadas, S. L. and Becker, E.: Numerical modeling of the generation of tertiary gravity waves in the mesosphere and thermosphere during strong mountain wave events over the southern Andes, J. Geophys. Res.-Space Phys., 124, 7687–7718, https://doi.org/10.1029/2019JA026694, 2019.

Vadas, S. L., Yue, J., She, C.-Y., Stamus, P. A., and Liu, A. Z.: A model study of the effects of winds on concentric rings of gravity waves from a convective plume near Fort Collins on 11 May 2004, J. Geophys. Res., 114, D06103, https://doi.org/10.1029/2008JD010753, 2009.

Vadas, S. L., Yue, J., and Nakamura, T.: Mesospheric concentric gravity waves generated by multiple convective storms over the North American Great Plains, J. Geophys. Res., 117, D07113, https://doi.org/10.1029/2011JD017025, 2012.

Visualization & Analysis Systems Technologies.: Geoscience Community Analysis Toolkit: WRF-Python [Software]. Boulder, CO: UCAR/NCAR - Computational and Informational System Lab. doi:10.5065/D6W094P1, 2017.

Wang, Z., Franke, J. A., Luo, Z., and Moyer, E. J.: Reanalyses and a high-resolution model fail to capture the “high tail” of CAPE distributions, Geophys. Res. Lett., 48, e2020GL091027, https://doi.org/10.1029/2020GL091027, 2021.

Weisman, M. L., Skamarock, W. C., and Klemp, J. B.: The resolution dependence of explicitly modeled convective systems, Mon. Weather Rev., 125, 527–548, https://doi.org/10.1175/1520-0493(1997)125<0527:TRDOEM>2.0.CO;2, 1997.

Yue, J., Vadas, S. L., She, C.-Y., Nakamura, T., Reising, S. C., Liu, H.-L., Stamus, P., Krueger, D. A., Lyons, W., and Li, T.: Concentric gravity waves in the mesosphere generated by deep convective plumes in the lower atmosphere near Fort Collins, Colorado, J. Geophys. Res., 114, D06104, https://doi.org/10.1029/2008JD011244, 2009.